

Application of Tilt Correlation Statistics to Anisoplanatic Optical Turbulence Modeling and Mitigation

RUSSELL C. HARDIE,^{1,*} MICHAEL A. RUCCI,²
SANTASRI BOSE-PILLAI,³ AND RICHARD VAN HOOK²

¹University of Dayton, Department of Electrical and Computer Engineering, 300 College Park, Dayton OH, USA, 45459-0232

²Air Force Research Laboratory, AFRL/RVMT, Building 620, 2241 Avionics Circle, Wright-Patterson AFB, Ohio, USA, 45433

³Air Force Institute of Technology, Department of Engineering Physics, 2950 Hobson Way, Dayton, Ohio, USA 45433

*Corresponding author: rhardie1@udayton.edu

Abstract: Atmospheric optical turbulence can be a significant source of image degradation, particularly in long range imaging applications. Many turbulence mitigation algorithms rely on an optical transfer function (OTF) model that includes the Fried parameter. We present anisoplanatic tilt statistics for spherical wave propagation. We transform these into 2D autocorrelation functions that can inform turbulence modeling and mitigation algorithms. Using these, we construct an OTF model that accounts for image registration. We also propose a spectral-ratio Fried parameter estimation algorithm that is robust to camera motion and requires no specialized scene content or sources. We employ the Fried parameter estimation and OTF model for turbulence mitigation. A numerical wave-propagation turbulence simulator is used to generate data to quantitatively validate the proposed methods. Results with real camera data are also presented.

© 2021 Optical Society of America

© 2021 Optical Society of America. One print or electronic copy may be made for personal use only. Systematic reproduction and distribution, duplication of any material in this paper for a fee or for commercial purposes, or modifications of the content of this paper are prohibited. <https://doi.org/10.1364/AO.418458>

1. Introduction

In long-range imaging, atmospheric optical turbulence can be a significant source of image degradation [1]. Therefore it is important to develop effective turbulence mitigation image restoration algorithms. In terrestrial imaging applications, a relative wide field-of-view is used. This leads to anisoplanatic conditions where the acquired short-exposure images are corrupted by spatially and temporally varying warp and blur. One simple and effective turbulence mitigation method is the Block Matching and Wiener Filtering (BMWF) algorithm [2, 3]. The BMWF method uses a Block Matching Algorithm (BMA) to perform dewarping on a sequence of short exposure frames. The dewarped frames are then fused in a temporal average or weighted average [4]. Image restoration with a Wiener filter is then applied to the fused image for deblurring purposes.

To specify the Wiener filter, a model for the optical transfer function (OTF) that relates the fused image to the undegraded truth image is required. We use a parametric OTF model here that relies on the atmospheric coherence diameter, r_0 , also referred to as the Fried parameter [5]. The Fried parameter governs the short-exposure atmospheric effects in the OTF model [5]. Our OTF model also takes into account how effective the image registration is in performing atmospheric tilt correction. For this, we define and use a parameter that we refer as the tilt

correction factor [2, 3]. In order to use a turbulence mitigation method such as the BMWF in an automated manner, we need to be able to estimate the Fried parameter from the observed images and separately determine the tilt correction factor. The main contribution of this paper is in the development of automated novel ways to obtain these two parameters, and utilize them for turbulence mitigation with the BMWF method.

There is a great deal of interest in characterizing atmospheric optical turbulence to help understand its impact on imaging and optical communications [6–10]. Thus, estimating the Fried parameter is important for many other applications in addition to the BMWF algorithm. This parameter can be measured with specialized equipment such as a scintillometer that monitors intensity fluctuations, or a differential image motion monitor [11] that uses a point source and two apertures. Some image-based methods have been developed that use a standard camera with specialized targets or sources [12, 13]. Other methods are scene-based and use only the natural imagery acquired by an imaging sensor [14–20]. Methods that explicitly address camera or scene motion include [9, 21].

In this paper, we present anisoplanatic tilt statistics for spherical wave propagation. Treating the tilts as wide sense stationary (WSS), we transform the tilt correlations into 2D autocorrelation functions that can inform modeling and mitigation algorithms. We use the 2D autocorrelation functions here to aid in forming our OTF model that captures the level of tilt correction provided by image registration. We use this OTF model to develop a modified spectral ratio Fried parameter estimation algorithm [17] that utilizes the full image, is robust to camera motion, and requires no specialized scene content or sources. The OTF model that employs the proposed Fried parameter estimation method is applied here for turbulence mitigation using the BMWF method. We evaluate the efficacy of the proposed Fried parameter estimation and turbulence mitigation using both simulated and real camera datasets. The simulated data are generated using the anisoplanatic numerical wave-propagation method developed by Hardie *et al* [22]. These data allow for quantitative performance analysis because ground truth images are available.

The organization of the remainder of this paper is as follows. In section 2, we introduce our turbulence mitigation approach as this sets the stage and provides motivation for the other contributions in this paper. Anisoplanatic tilt correlation statistics are presented in Section 3. The application of the tilt statistics to turbulence OTF modeling with image registration is developed in Section 4. This leads to our proposed spectral-ratio Fried parameter estimation method in Section 5. Experimental results are presented in Section 6. Finally, we offer conclusions in Section 7.

2. Turbulence Mitigation

A block diagram of the BMWF [2] turbulence mitigation algorithm used here is shown in Fig. 1. The basic idea of BMWF is to use image registration to perform dewarping and then Wiener filtering to deblur. The observed frames are denoted $f_k(x, y)$ for $k = 1, 2, \dots, K$, where x, y are spatial coordinates and k is the temporal frame index. The ideal image is assumed to be $z(x, y)$ and the estimate formed is denoted $\hat{z}(x, y)$.

The first step illustrated in Fig. 1 is to form a prototype image with the approximately correct geometry from the observed frames. Because the warping shifts have a zero-mean, a simple average of the observed frames often produces a useful prototype [2, 23]. This prototype is effectively a long exposure image. It has improved geometry compared with individual frames, but has a significant amount of turbulence motion blur as well. Global registration may be applied here prior to averaging to reduce some of the blurring and compensate for camera motion. To further reduce turbulence motion blur, the individual observed frames are registered to the prototype using a BMA. Let the BMA block size be defined as $(2M + 1) \times (2M + 1)$, for integer parameter M . The BMA registered images are then fused with a simple average to form the image $f(x, y)$ as shown in Fig. 1. Other fusion options are also possible [4]. Note that $f(x, y)$

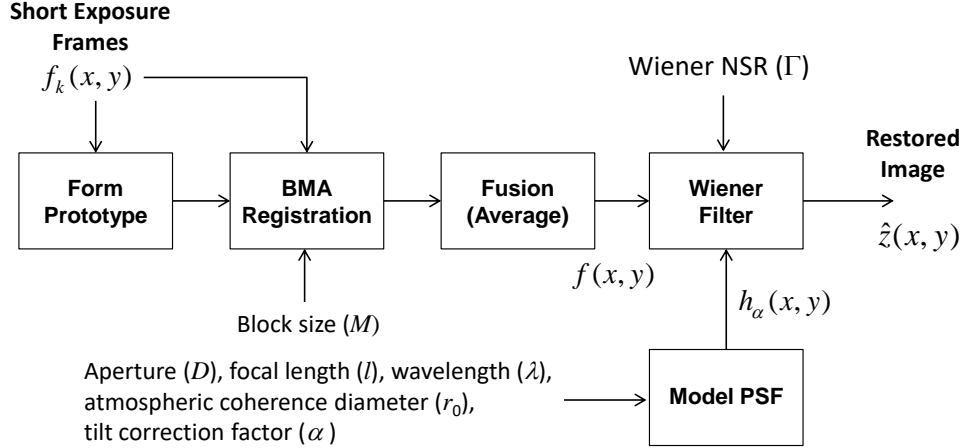


Fig. 1. Block matching and Wiener filtering turbulence mitigation system block diagram [2].

should have significantly less motion blurring than the prototype because of the BMA registration. Ideally, the BMA registration would perfectly compensate for the turbulence warping. However, as explained by Hardie *et al* [2], any finite-size block registration method will provide only partial tilt correction because of the patch averaging effect [19, 20].

Following the original BMWF development [2], we shall model the fused image $f(x, y)$ as

$$f(x, y) = h_\alpha(x, y) * z(x, y) + \eta(x, y), \quad (1)$$

where $h_\alpha(x, y)$ is a linear shift invariant (LSI) point spread function (PSF) that accounts for diffraction, the average short-exposure atmospheric blurring, and residual turbulence motion blur [2]. The term $\eta(x, y)$ is assumed to be additive Gaussian noise. In the spatial frequency domain, the model is expressed as

$$F(u, v) = H_\alpha(u, v)Z(u, v) + N(u, v), \quad (2)$$

where u, v are spatial frequency variables. The degradation OTF is given by

$$H_\alpha(u, v) = FT\{h_\alpha(x, y)\}, \quad (3)$$

where $FT\{\cdot\}$ represents the 2D Fourier transform. The frequency spectrum of the ideal image, fused image, and noise are given by $Z(u, v)$, $F(u, v)$, and $N(u, v)$, respectively. What makes this model different from traditional approaches is that it includes impact of the BMA registration on the fused image $f(x, y)$. This unique feature is captured by the parameter α that we refer to as the tilt correction factor [2]. It provides a measure of how effective the BMA registration is at compensating for the warping from turbulence tilt variance. We formally define α in Section 3 and provide details on the blurring model expressed in Eqs. (1) and (2) in Section 4.

Finally, we see in Fig. 1 that a Wiener filter is used to deconvolve the LSI blurring from Eq. (1). The frequency response of the Wiener [24] filter is given by

$$H_W(u, v) = \frac{H_\alpha(u, v)^*}{|H_\alpha(u, v)|^2 + \Gamma}, \quad (4)$$

where Γ represents a constant noise-to-signal (NSR) power spectral density ratio. The final spatial domain BMWF estimate can then be expressed as

$$\hat{z}(x, y) = FT^{-1}(H_W(u, v)F(u, v)). \quad (5)$$

In practice, Eq. (5) is computed in discrete space using the fast Fourier transform (FFT) [25].

The key to the BMWF method is the PSF model used in Eq. (1), or equivalently the OTF model in Eq. (2). As we will see in Section 4, this model depends on optical parameters, Fried parameter r_0 [5], and the BMA tilt correction factor α [2]. The optical parameters are generally known for a given imaging system. Thus, the challenge in modeling the blurring PSF/OTF is in estimating α and r_0 . The main contribution of this paper is the presentation and analysis of new methods to estimate these two parameters from a sequence of short exposure images. We will present a method in Section 3.3 that computes α only from knowledge of key optical parameters and the block size parameter M . Next, we present a modified spectral ratio method to estimate r_0 in Section 5. This method uses α and a sequence of short exposure images. One of the novel features of the proposed r_0 estimation method relates to how we address camera motion and image registration using α . Furthermore, it utilizes the full image size and does not require any specialized sources or target images. Our approaches for computing α and estimating r_0 rely on anisoplanatic tilt correlation statistics. Thus, we turn our attention to these statistics in the following section.

3. Anisoplanatic Tilt Correlation Statistics

3.1. Parallel and Perpendicular Separation Tilt Correlations

Let the two-axis Zernike-tilt (Z-tilt) angle vector be expressed as $\tilde{\mathbf{z}}(\boldsymbol{\theta}) = [\tilde{z}_x(\boldsymbol{\theta}), \tilde{z}_y(\boldsymbol{\theta})]^T$ for a point source originating from an angle of $\boldsymbol{\theta} = [\theta_x, \theta_y]^T$. For a spherical wave characterized by the Kolmogorov power spectrum, the tilt correlation has been derived by Basu (now Bose-Pillai) *et al* [9, 19] using methods based on those by Fried [26] and Winick [27]. The result for the total tilt correlation for two point sources originating from angles $\boldsymbol{\theta}_1$ and $\boldsymbol{\theta}_2$ is given by

$$\begin{aligned} \tilde{r}_T(\boldsymbol{\theta}) &= \langle \tilde{\mathbf{z}}(\boldsymbol{\theta}_1) \cdot \tilde{\mathbf{z}}(\boldsymbol{\theta}_2) \rangle = \langle \tilde{z}_x(\boldsymbol{\theta}_1)\tilde{z}_x(\boldsymbol{\theta}_2) + \tilde{z}_y(\boldsymbol{\theta}_1)\tilde{z}_y(\boldsymbol{\theta}_2) \rangle = \\ &= \left(-\frac{2.91}{2}\right) \left(\frac{16}{\pi}\right)^2 D^{-1/3} \int_{z=0}^L C_n^2(z) \int_{\vartheta=0}^{2\pi} \int_{u=0}^1 \left[u \cos^{-1}(u) - u^2 (3 - 2u^2) \sqrt{1 - u^2} \right] \times, \quad (6) \\ & \left[u^2 \left(\frac{z}{L}\right)^2 + \left(\frac{L-z}{D}\theta\right)^2 + 2u \left(\frac{z}{L}\right) \left(\frac{L-z}{D}\theta\right) \cos(\vartheta) \right]^{5/6} dud\vartheta dz \end{aligned}$$

where $\theta = |\boldsymbol{\theta}_1 - \boldsymbol{\theta}_2|$ is the angular source separation, D is the aperture diameter, L is the optical path length, and $C_n^2(z)$ is the refractive index structure parameter with $z = 0$ at the source. Note that $\langle \cdot \rangle$ represents an ensemble mean operator. The tilt correlation as a function of separation angle in the direction parallel to the source separation can be shown to be

$$\begin{aligned} \tilde{r}_{\parallel}(\boldsymbol{\theta}) &= \left(-\frac{2.91}{8}\right) \left(\frac{64}{\pi}\right)^2 D^{-1/3} \int_{z=0}^L C_n^2(z) \int_{\vartheta=0}^{2\pi} \int_{u=0}^1 \left[\left(\frac{1}{8}u \cos^{-1}(u)\right) + u \sqrt{1 - u^2} \left(\frac{1}{12}u^3 - \frac{5}{24}u\right) \right. \\ & \left. + u \sqrt{1 - u^2} \left(\frac{u^3 - u}{3}\right) \cos^2(\vartheta) \right] \times \left[u^2 \left(\frac{z}{L}\right)^2 + \left(\frac{L-z}{D}\theta\right)^2 + 2u \left(\frac{z}{L}\right) \left(\frac{L-z}{D}\theta\right) \cos(\vartheta) \right]^{5/6} dud\vartheta dz \quad (7) \end{aligned}$$

Similarly, the tilt correlation as a function of separation angle in the direction perpendicular to the source separation is given by

$$\begin{aligned} \tilde{r}_{\perp}(\boldsymbol{\theta}) &= \left(-\frac{2.91}{8}\right) \left(\frac{64}{\pi}\right)^2 D^{-1/3} \int_{z=0}^L C_n^2(z) \int_{\vartheta=0}^{2\pi} \int_{u=0}^1 \left[\left(\frac{1}{8}u \cos^{-1}(u)\right) + u \sqrt{1 - u^2} \left(\frac{1}{12}u^3 - \frac{5}{24}u\right) \right. \\ & \left. + u \sqrt{1 - u^2} \left(\frac{u^3 - u}{3}\right) \sin^2(\vartheta) \right] \times \left[u^2 \left(\frac{z}{L}\right)^2 + \left(\frac{L-z}{D}\theta\right)^2 + 2u \left(\frac{z}{L}\right) \left(\frac{L-z}{D}\theta\right) \cos(\vartheta) \right]^{5/6} dud\vartheta dz \quad (8) \end{aligned}$$

The total tilt correlation in Eq. (6) is related the expressions in Eqs. (7) and (8) by

$$\tilde{r}_T(\boldsymbol{\theta}) = \tilde{r}_{\parallel}(\boldsymbol{\theta}) + \tilde{r}_{\perp}(\boldsymbol{\theta}). \quad (9)$$

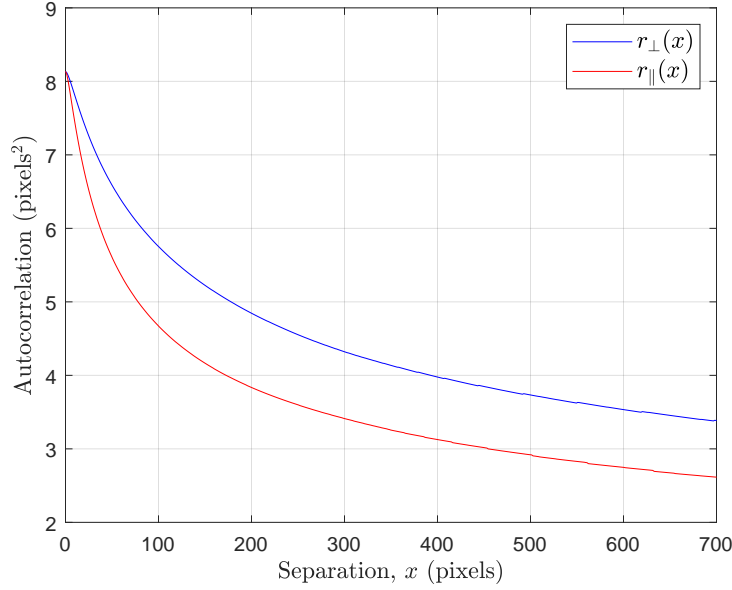


Fig. 2. Tilt correlations for two point sources as a function of perpendicular and parallel separation in pixel spacings for the optical parameters in Table 1 and a constant $C_n^2(z) = 1.0 \times 10^{-15} \text{ m}^{-2/3}$.

Note that the one-axis Z-tilt variance in units of radians squared is given by Eqs. (7) and (8) evaluated at a separation angle of 0 yielding

$$\tilde{\sigma}_T^2 = \tilde{r}_{\parallel}(0) = \tilde{r}_{\perp}(0) = \tilde{r}_T(0)/2. \quad (10)$$

The tilt correlations can be expressed in terms of separation in pixel spacings using the scaling $r_{\parallel}(x) = \tilde{r}_{\parallel}(\xi x) / \xi^2$ and $r_{\perp}(x) = \tilde{r}_{\perp}(\xi x) / \xi^2$, where ξ represents the angle subtended by one pixel. Therefore the one-axis Z-tilt variance in units of pixel spacings squared is given by

$$\sigma_T^2 = r_{\parallel}(0) = r_{\perp}(0) = r_T(0)/2. \quad (11)$$

A pair of the tilt correlation functions is plotted in Fig. 2 for the optical parameters listed in Table 1 and a constant $C_n^2(z) = 1.0 \times 10^{-15} \text{ m}^{-2/3}$. Note that the perpendicular separation shows higher correlation than the parallel separation. To understand this phenomenon, it may be helpful to consider Fig. 3. Depicted there are isocontours of spherical waves propagating from two point sources at a given distance from the camera. Note that the two paths share more of the random medium in common in the perpendicular direction than the parallel direction (i.e., the blue arrow is longer than the red). This is the basis for the asymmetry in the correlation statistics.

3.2. 2D Correlation Functions

From a statistical signal processing standpoint, it is more convenient to transform the parallel and perpendicular tilt correlations into more traditional 2D autocorrelation functions, treating them as WSS. This can be done in a fashion similar to that presented by Schwartzman *et al* [28]. However, here we use the tilt correlation statistics from Bose-Pillai *et al* [9, 19] that have been validated with our anisoplanatic turbulence simulator [22].

To derive this mapping, consider the two tilt vectors depicted in Fig. 4 in the image plane. Let the spatial coordinates of the sources be represented in units of pixels. Without loss of generality, let one of the sources be located at the origin $\mathbf{0} = [0, 0]^T$ and the other at $\mathbf{n} = [n_1, n_2]^T$. These two

Table 1. Optical parameters used for the example and simulation results.

Parameter	Value
Aperture	$D = 0.2034$ m
Focal length	$l = 1.2$ m
F-number	$f/\# = 5.9$
Wavelength	$\lambda = 0.525$ μm
Object distance	$L = 7$ km
Nyquist pixel spacing (focal plane)	$\delta = 1.5488$ μm
Nyquist pixel angle	$\xi = 1.2906 \times 10^{-6}$ rad

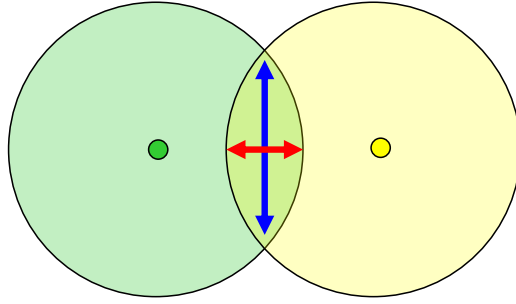


Fig. 3. Isocontours of spherical waves propagating from two point sources at a given distance from the camera. The two paths share more of the random medium in common in the perpendicular direction than the parallel direction, giving rise to non-isotropic correlation statistics.

sources are separated by a distance of $d(\mathbf{n}) = \sqrt{n_1^2 + n_2^2}$. The angle of a line connecting the two sources, relative to the horizontal axis of the camera focal plane array, is $\phi(\mathbf{n}) = \tan^{-1}(n_2/n_1)$. The tilt vectors in the image plane for these two point sources are represented as $\mathbf{z}(\mathbf{0})$ and $\mathbf{z}(\mathbf{n})$, respectively. These tilt vectors can be expressed in terms of parallel and perpendicular components shown in green, as well as x and y components shown in blue. Using a coordinate transformation of the vector components, via vector projection, these two forms can be related by

$$z_x(\mathbf{n}) = z_{\parallel}(\mathbf{n}) \cos(\phi(\mathbf{n})) - z_{\perp}(\mathbf{n}) \sin(\phi(\mathbf{n})) \quad (12)$$

and

$$z_y(\mathbf{n}) = z_{\parallel}(\mathbf{n}) \sin(\phi(\mathbf{n})) + z_{\perp}(\mathbf{n}) \cos(\phi(\mathbf{n})). \quad (13)$$

Using Eqs. (12) and (13) and noting that the cross-correlation between the parallel and perpendicular components is zero, we obtain the 2D correlation functions shown below. The 2D autocorrelation for the horizontal axis tilt correlation is given by

$$r_{xx}(\mathbf{n}) = E [z_x(\mathbf{0})z_x(\mathbf{n})] = r_{\parallel}(d(\mathbf{n})) \cos^2(\phi(\mathbf{n})) + r_{\perp}(d(\mathbf{n})) [1 - \cos^2(\phi(\mathbf{n}))]. \quad (14)$$

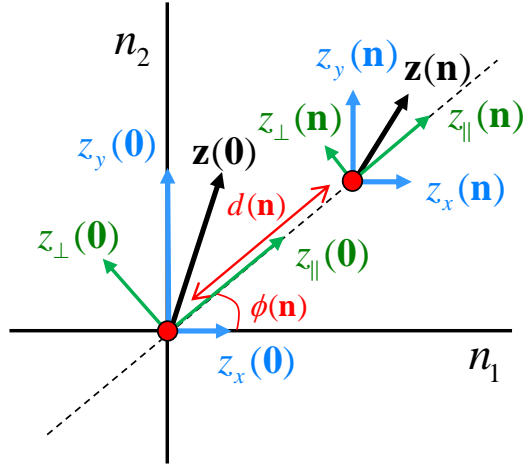


Fig. 4. Geometry for mapping parallel and perpendicular tilt correlations to 2D x and y tilt autocorrelation functions. Two point sources (red) are shown in the image plane. The tilt vectors are shown as $\mathbf{z}(\mathbf{0})$ and $\mathbf{z}(\mathbf{n})$. These can be expressed in terms of parallel and perpendicular components (green), or x and y components (blue).

Similarly the 2D autocorrelation for the vertical axis tilt correlation is given by

$$r_{yy}(\mathbf{n}) = E [z_y(\mathbf{0})z_y(\mathbf{n})] = r_{\parallel}(d(\mathbf{n})) \sin^2(\phi(\mathbf{n})) + r_{\perp}(d(\mathbf{n})) [1 - \sin^2(\phi(\mathbf{n}))]. \quad (15)$$

The total of the x and y autocorrelations is the sum

$$r_T(\mathbf{n}) = r_{xx}(\mathbf{n}) + r_{yy}(\mathbf{n}) = \tilde{r}_T(\xi d(\mathbf{n})) / \xi^2. \quad (16)$$

Finally, the cross-correlation is given by

$$r_{xy}(\mathbf{n}) = r_{yx}(\mathbf{n}) = E [z_x(\mathbf{0})z_y(\mathbf{n})] = (r_{\parallel}(d(\mathbf{n})) - r_{\perp}(d(\mathbf{n}))) \cos(\phi(\mathbf{n})) \sin(\phi(\mathbf{n})). \quad (17)$$

Applying these transformations to the data in Fig. 2 produces the 2D correlation functions shown in Fig. 5. Note that the one-axis Z-tilt variance in units of pixels squared is given by $\sigma_T^2 = r_{xx}(\mathbf{0}) = r_{yy}(\mathbf{0}) = r_T(\mathbf{0})/2$.

3.3. Tilt Correction Using Image Patch Registration

Formulating the 2D tilt autocorrelation functions, as done in Section 3.2, allows us to conveniently take advantage of a number of well known statistical signal processing relationships. In particular, we are interested in understanding how image registration impacts the tilt statistics. Our idea here is that we can model the impact of image registration as filtering random tilt fields with an LSI filter and adding a measurement error term. Consider processing a WSS x -dimension random tilt field using an LSI filter with impulse response $h(\mathbf{n})$. This is denoted as

$$\bar{z}_x(\mathbf{n}) = z_x(\mathbf{n}) * h(\mathbf{n}) + e_x(\mathbf{n}), \quad (18)$$

where $e_x(\mathbf{n})$ is the measurement error associated with the x tilt at position \mathbf{n} . Let us treat the measurement error as zero-mean independent and identically distributed white noise with standard deviation σ_e in units of pixel spacings. In this case, the output autocorrelation can be expressed as

$$\bar{r}_{xx}(\mathbf{n}) = r_{xx}(\mathbf{n}) * h(\mathbf{n}) * h(-\mathbf{n}) + \sigma_e^2 \delta(\mathbf{n}), \quad (19)$$

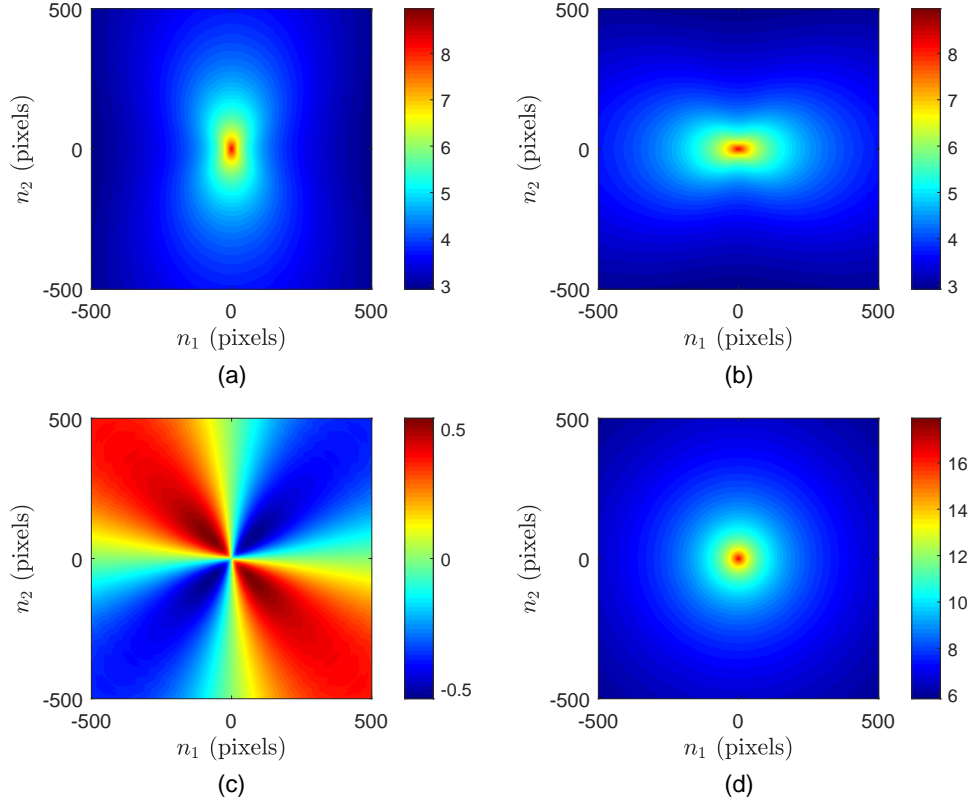


Fig. 5. 2D tilt correlation functions corresponding to the statistics shown in Fig. 2 using Eqs. (14) - (17). (a) $r_{xx}(\mathbf{n})$, (b) $r_{yy}(\mathbf{n})$, (c) $r_{xy}(\mathbf{n}) = r_{yx}(\mathbf{n})$ and (d) $r_T(\mathbf{n}) = r_{xx}(\mathbf{n}) + r_{yy}(\mathbf{n})$.

or equivalently

$$\bar{r}_{xx}(\mathbf{n}) = \sigma_e^2 \delta(\mathbf{n}) + \sum_{\mathbf{m}} \sum_{\mathbf{k}} h(\mathbf{m}) h(\mathbf{k}) r_{xx}(\mathbf{n} + \mathbf{m} - \mathbf{k}, \mathbf{n} + \mathbf{m} - \mathbf{k}), \quad (20)$$

where $\mathbf{m} = [m_1, m_2]^T$, $\mathbf{k} = [k_1, k_2]^T$, and $\delta(\mathbf{n})$ is a 2D Kronecker delta function. The variance of the processed random tilt field is given by

$$\bar{\sigma}_{xx}^2 = \bar{r}_{xx}(\mathbf{0}) = \sigma_e^2 + \sum_{\mathbf{m}} \sum_{\mathbf{k}} h(\mathbf{m}) h(\mathbf{k}) r_{xx}(\mathbf{m} - \mathbf{k}, \mathbf{m} - \mathbf{k}). \quad (21)$$

Of course, the same can be done for the y -dimension tilt to produce $\bar{r}_{yy}(\mathbf{n})$ and $\bar{\sigma}_{yy}^2$ from $r_{yy}(\mathbf{n})$. Note that if the filter impulse response is isotropic in x and y , the tilt variance result will be the same whether you use $r_{xx}(\mathbf{n})$, $r_{yy}(\mathbf{n})$, or $r_T(\mathbf{n})/2$. That is, in the isotropic case, $\bar{\sigma}_{yy}^2 = \bar{\sigma}_{xx}^2$. For non-isotropic filters, the impact of the filtering on the x and y tilt variance must be computed separately.

Now let us consider the special case of averaging the tilts over a square patch with side dimension of $2M + 1$. This is equivalent to applying a moving average filter to the tilt fields with

impulse response

$$h_P(\mathbf{n}) = \begin{cases} \frac{1}{(2M+1)^2} & |n_1|, |n_2| \leq M \\ 0 & \text{otherwise} \end{cases}. \quad (22)$$

Using this impulse response plugged into Eqs. (19) or (20) and including measurement error gives the output tilt correlation function for estimated patch tilt. It can be applied to $r_{xx}(\mathbf{n})$, $r_{yy}(\mathbf{n})$, or $r_T(\mathbf{n})$. Combining Eqs. (21) and (22) gives the variance of estimated square-patch tilt as

$$\sigma_P^2 = \sigma_e^2 + \frac{1}{(2M+1)^4} \sum_{\mathbf{m}=-M\mathbf{1}}^{M\mathbf{1}} \sum_{\mathbf{k}=-M\mathbf{1}}^{M\mathbf{1}} r_{xx}(\mathbf{m}-\mathbf{k}, \mathbf{m}-\mathbf{k}), \quad (23)$$

where $\mathbf{1} = [1, 1]^T$. Because the moving average filter is isotropic, one could equivalently use $r_{xx}(\mathbf{n})$, $r_{yy}(\mathbf{n})$, or $r_T(\mathbf{n})/2$ in Eq. (23).

To model the patch-based image registration that attempts to correct for these patch tilts, we propose using an identity filter minus a moving average filter. The output of this difference filter represents the residual tilt after registration. The residual tilt impulse response for a $2M+1$ square patch size is

$$h_R(\mathbf{n}) = \delta(\mathbf{n}) - h_P(\mathbf{n}). \quad (24)$$

Using this impulse response plugged into Eqs. (19) or (20) gives the output tilt correlation function after the patch registration. As with the patch tilt correlations, we can obtain the post-registration residual tilt statistics corresponding to $r_{xx}(\mathbf{n})$, $r_{yy}(\mathbf{n})$, or $r_T(\mathbf{n})$. Examples of the correlation functions from Fig. 5 after filtering with $h_R(\mathbf{n})$ for $M=50$ (i.e., 101×101 patch tilt correction) are shown in Fig. 6 for $\sigma_e=0$. Looking at the vertical colorbar scales, one can see that the residual tilt variance is greatly reduced compared with Fig. 5 as a result of such a registration process.

The residual tilt variance can then be computed as a function of block size using the impulse response in Eq. (24) and the relationship in Eq. (21) yielding

$$\sigma_R^2 = \sigma_e^2 + \sum_{\mathbf{m}=-M\mathbf{1}}^{M\mathbf{1}} \sum_{\mathbf{k}=-M\mathbf{1}}^{M\mathbf{1}} h_R(\mathbf{m})h_R(\mathbf{k})r_{xx}(\mathbf{m}-\mathbf{k}, \mathbf{m}-\mathbf{k}). \quad (25)$$

The patch tilt variance, σ_P^2 , and residual tilt variance, σ_R^2 , are plotted in Fig. 7 as a function of the square patch half width M for $\sigma_e=0$. These correspond to the optical parameters in Table 1 and $C_n^2(z) = 1.0 \times 10^{-15} \text{ m}^{-2/3}$. Also shown is the original unprocessed tilt variance σ_T^2 . Note that as the patch size increases, the patch tilt variance decreases, and the residual tilt variance increases. We can quantify the level of tilt variance reduction accomplished by the patch registration by comparing the residual tilt variance σ_R^2 to the total input tilt variance σ_T^2 . In particular, we define the tilt correction factor as

$$\alpha = 1 - \frac{\sigma_R^2}{\sigma_T^2} = 1 - \varepsilon - \frac{1}{r_{xx}(\mathbf{0})} \sum_{\mathbf{m}=-M\mathbf{1}}^{M\mathbf{1}} \sum_{\mathbf{k}=-M\mathbf{1}}^{M\mathbf{1}} h_R(\mathbf{m})h_R(\mathbf{k})r_{xx}(\mathbf{m}-\mathbf{k}, \mathbf{m}-\mathbf{k}), \quad (26)$$

where $\varepsilon = \sigma_e^2/\sigma_T^2$ is the registration error-to-signal ratio. Again, note that we use the relationship $\sigma_T^2 = r_{xx}(\mathbf{0})$ in expressing Eq. (26). Also, note that the autocorrelation function $r_{xx}(\mathbf{n})$ is derived from the correlations in Eqs. (6) - (8). These correlations are a function of $C_n^2(z)$. However, when $C_n^2(z)$ is constant, it can be brought out of all of the integrals. Since the rightmost term in Eq. (26) has $r_{xx}(\cdot)$ in the numerator and denominator, this constant will cancel. If we further assume ε is constant, then α is not a function of turbulence strength. This means that for constant $C_n^2(z)$, the tilt correction factor is only a function of camera parameters, optical path

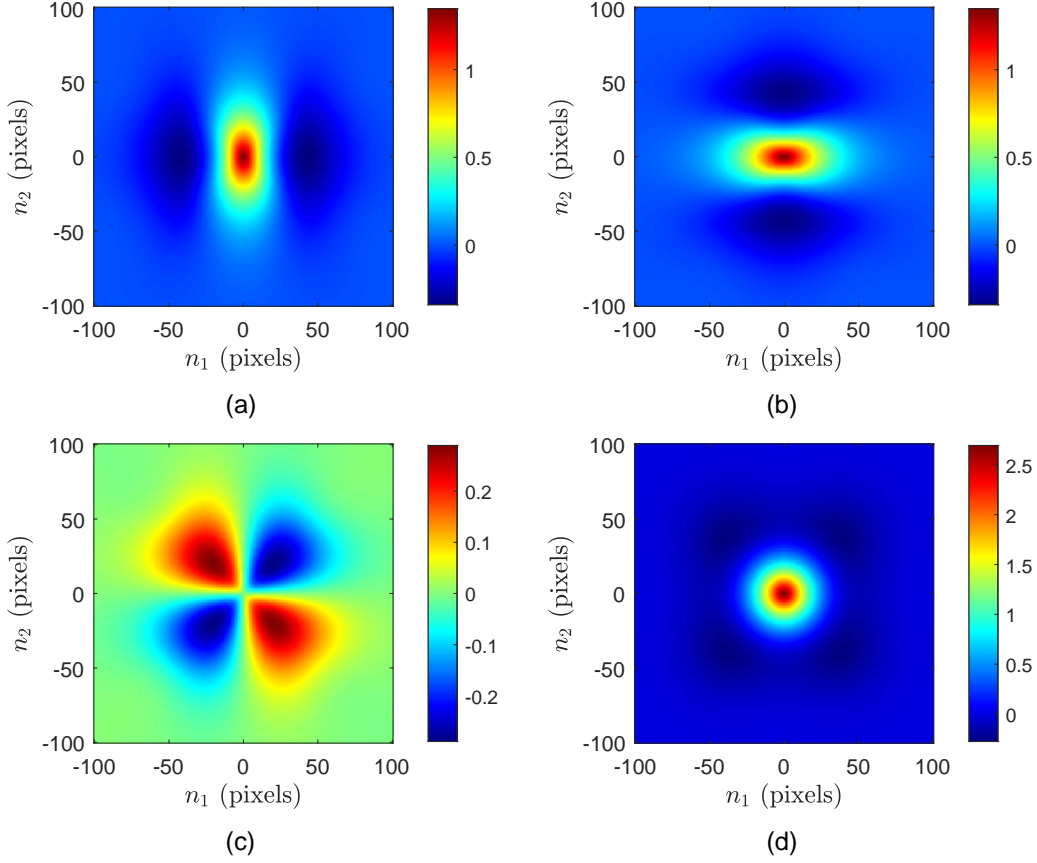


Fig. 6. 2D residual tilt correlation functions corresponding to those in Fig. 5 after filtering the tilt fields using the impulse response in Eq. (24) for $M = 50$ (i.e., 101×101 patch tilt correction). (a) $\bar{r}_{xx}(\mathbf{n})$, (b) $\bar{r}_{yy}(\mathbf{n})$, (c) $\bar{r}_{xy}(\mathbf{n}) = \bar{r}_{yx}(\mathbf{n})$ and (d) $\bar{r}_T(\mathbf{n}) = \bar{r}_{xx}(\mathbf{n}) + \bar{r}_{yy}(\mathbf{n})$.

length, and the patch size M . Thus, in this case we can compute α without *a priori* knowledge of the turbulence strength.

Note that the tilt correction factor α generally ranges from 0 to 1. However, it is possible for this parameter to become negative if the residual tilt variance, σ_R^2 , is larger than the input tilt variance, σ_T^2 . This would imply that error in the registration is larger than any tilt correction being performed, resulting in a net increase in tilt variance. It would be advisable in this scenario to forgo such ineffective registration if the goal is to reduce tilt variance.

The tilt correction factor for the parameters in Table 1 and $C_n^2(z) = 1.0 \times 10^{-15} \text{ m}^{-2/3}$ is plotted as a function of M in Fig. 8 for $\varepsilon = 0$. For large M , only large scale low-frequency tilts are corrected, giving rise to a relatively small tilt correction factor. However, large patch tilts can be estimated much more accurately than smaller ones because of the number of image pixels involved. As M decreases, the turbulence warping compensation is occurring on a smaller spatial scale, leaving less residual tilt variance, and generating more tilt correction.

We have also conducted a sensitivity analysis to see the impact of a non-constant $C_n^2(z)$ profile on α . The results are summarize in Fig. 9. In this analysis we consider a linear $C_n^2(z)$ profile with an average value of $C_n^2 = 1 \times 10^{-15} \text{ m}^{-2/3}$ and source-to-camera change of ΔC_n^2 . Shown in Fig. 9

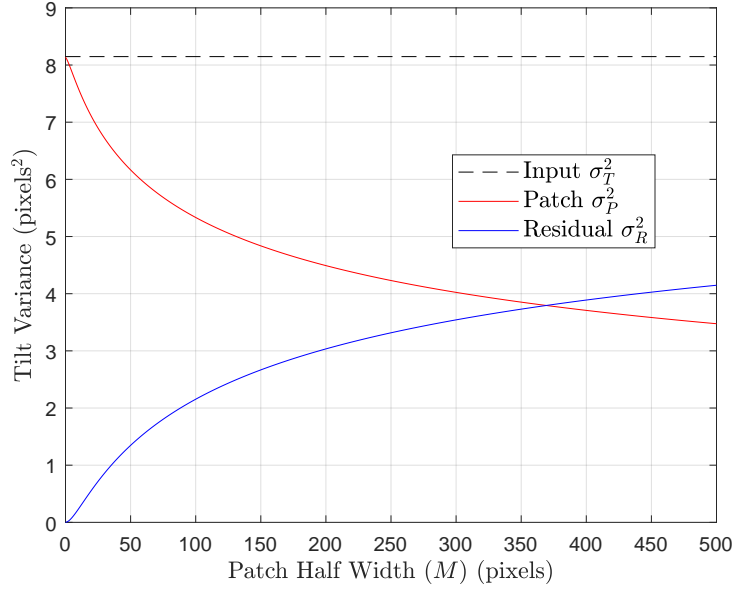


Fig. 7. Tilt variances as a function of patch half width M for the optical parameters in Table 1 and $C_n^2(z) = 1.0 \times 10^{-15} \text{ m}^{-2/3}$. Shown are the constant input tilt variance σ_T^2 , the patch tilt variance σ_P^2 , and the residual tilt variance σ_R^2 .

are the true α values for the varying $C_n^2(z)$ path for four values of M with $\varepsilon = 0$. Also shown are the corresponding values obtained assuming a constant C_n^2 . Note that for $\Delta C_n^2 = -2 \times 10^{-15}$, we have strong turbulence at the source, and no turbulence at the camera. In this case, the true path-dependent α is lower than what is predicted using a constant path assumption. This means the registration will be less effective in tilt correction than the constant path prediction. Object-heavy turbulence gives rise to a lower isoplanatic angle and more localized warping [22]. Thus, it stands to reason that block-based registration would be less effective in this scenario. Note that the sensitivity illustrated in Fig. 9 is reduced with smaller values of M .

3.4. Tilt Correction with Global Registration

In the previous section, we considered patch-based image registration such as the BMA for tilt reduction. However, it is also interesting to apply this tilt autocorrelation function analysis to the scenario of global image registration. The global registration effectively seeks to determine the average tilt across the full image and then correct all pixels with this one global shift. Thus, imagine a patch filter $h_P(\mathbf{n})$ where $2M + 1$ spans the full image size. Such a filter outputs the global average tilt shifts. The correction filter would no longer be spatially invariant as we used in Eq. (24). Rather, the residual filter would vary with each pixel's location $\mathbf{k} = [k_1, k_2]^T$, yielding

$$h_R(\mathbf{n}; \mathbf{k}) = \delta(\mathbf{n} + \mathbf{k}) - h_P(\mathbf{n}). \quad (27)$$

The residual tilt variance can now be computed in a fashion similar to that in Eq. (25). Because the filter in Eq. (27) is non-isotropic, the residual tilt variance in x and y must be computed separately using the corresponding tilt correlation function. Furthermore, the residual tilt variance must be computed separately for each pixel \mathbf{k} . We can use the residual tilt variance along with the total tilt variance to form a tilt correction factor similar to that in Eq. (26). However, now the tilt correction factor is a function of pixel position and is different in x and y .

These global tilt correction factor functions are plotted in Fig. 10 for $M = 250$ with the optical

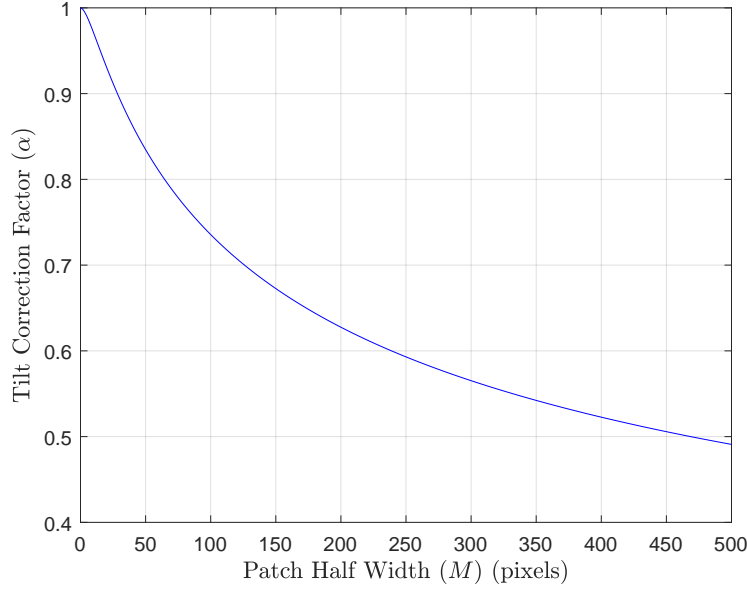


Fig. 8. Tilt correction factor α as a function of M for the optical parameters in Table 1, $\varepsilon = 0$, and any constant C_n^2 . Using a larger registration patch provides less tilt correction, but larger patches can yield a more accurate motion estimate.

parameters in Table 1. Note that there is more tilt correction in the center of the image and less in the corners. This behavior is explained by the fact that global registration will be most representative of the bulk of the image that is contained in the center. The global shifts are least representative of the corners. Notwithstanding this spatially varying relationship, we have observed that useful results in our parameter estimation problems can be achieved by using the average tilt correction factor and neglecting the spatial variation. Note in Fig. 10 that the peak value of the two surfaces is 0.5903 which matches Fig. 8 for $M = 250$. The tilt reduction factor obtained by averaging over all pixels is $\alpha = 0.5181$.

4. Application to Turbulence OTF Modeling

Let us now turn our attention to defining the OTF in the observation model introduced in Eqs. (1) and (2). In our model we shall include the effects of diffraction-limited optics, the average short exposure atmospheric OTF, and the averaging of frames with residual tilt variance [2, 3]. The OTF combining these components is given by

$$H_\alpha(\rho) = H_{\text{dif}}(\rho)H_{\text{SE}}(\rho)G_\alpha(\rho), \quad (28)$$

where $H_{\text{dif}}(\rho)$ is for diffraction-limited optics, $H_{\text{SE}}(\rho)$ is the average short-exposure OTF, and $G_\alpha(\rho)$ captures blurring from averaging frames with residual tilt variance. These component functions are circularly symmetric and the radial frequency parameter $\rho = \sqrt{u^2 + v^2}$, where u and v are the spatial frequencies in units of cycles per unit distance in the camera focal plane.

The diffraction-limited OTF for a circular exit pupil [29] is given by

$$H_{\text{dif}}(\rho) = \begin{cases} \frac{2}{\pi} \left[\cos^{-1} \left(\frac{\rho}{2\rho_c} \right) - \frac{\rho}{2\rho_c} \sqrt{1 - \left(\frac{\rho}{2\rho_c} \right)^2} \right] & \rho \leq \rho_c \\ 0 & \text{otherwise} \end{cases}, \quad (29)$$

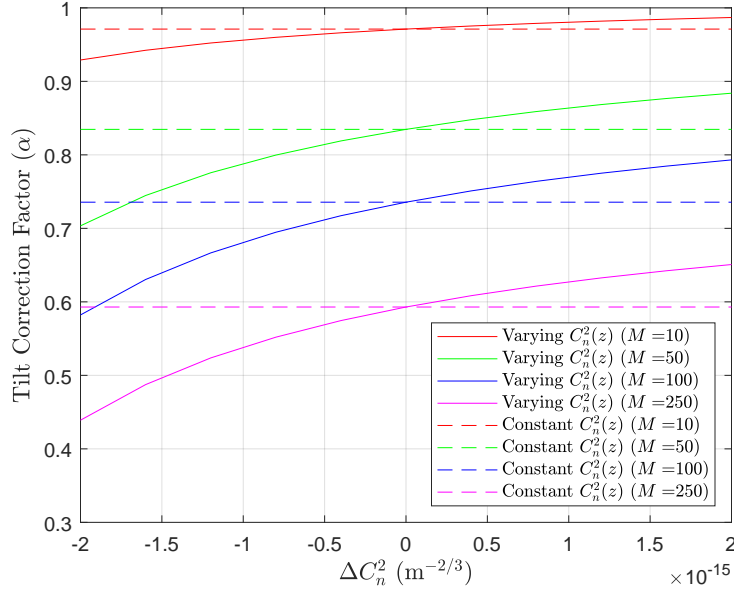


Fig. 9. Tilt correction factor α as a function of the source-to-camera change for a linear $C_n^2(z)$ profile using the optical parameters in Table 1 and $\varepsilon = 0$. The path average value is $C_n^2 = 1 \times 10^{-15} \text{ m}^{-2/3}$.

where $\rho_c = 1/(\lambda f/\#)$ is the optical cut-off frequency, and the f-number is $f/\# = l/D$. For the average short exposure OTF, we will use Fried's near-field model based on Kolmogorov statistics [1, 5]. This is given by

$$H_{\text{SE}}(\rho) = \exp \left\{ -3.44 \left(\frac{\lambda \rho}{r_0} \right)^{5/3} \left[1 - \left(\frac{\lambda \rho}{D} \right)^{1/3} \right] \right\}. \quad (30)$$

Fried [5] states that the near-field approximation is for $D \gg \sqrt{L\lambda}$. However, Tofsted [30–32] showed that this approximation is quite good even up to $D \approx \sqrt{L\lambda}$.

The term $G_\alpha(\rho)$ is a Gaussian function that corresponds to blurring from residual tilt variance. We wish to define this function so that when $\alpha = 0$ (no tilt correction) we have

$$H_{\text{SE}}(\rho)G_0(\rho) = H_{\text{LE}}(\rho), \quad (31)$$

where $H_{\text{LE}}(\rho)$ is Fried's long exposure OTF model [1, 5] given by

$$H_{\text{LE}}(\rho) = \exp \left\{ -3.44 \left(\frac{\lambda \rho}{r_0} \right)^{5/3} \right\}. \quad (32)$$

Also, for $\alpha = 1$ (perfect tilt correction), we want $G_1(\rho) = 1$ so that

$$H_{\text{SE}}(\rho)G_1(\rho) = H_{\text{SE}}(\rho). \quad (33)$$

As shown by Hardie *et al* [2], we can achieve this using the relationship

$$G_\alpha(\rho) = \exp \left\{ -\frac{3.44(1-\alpha)(\lambda \rho)^2}{r_0^{5/3} D^{1/3}} \right\}. \quad (34)$$

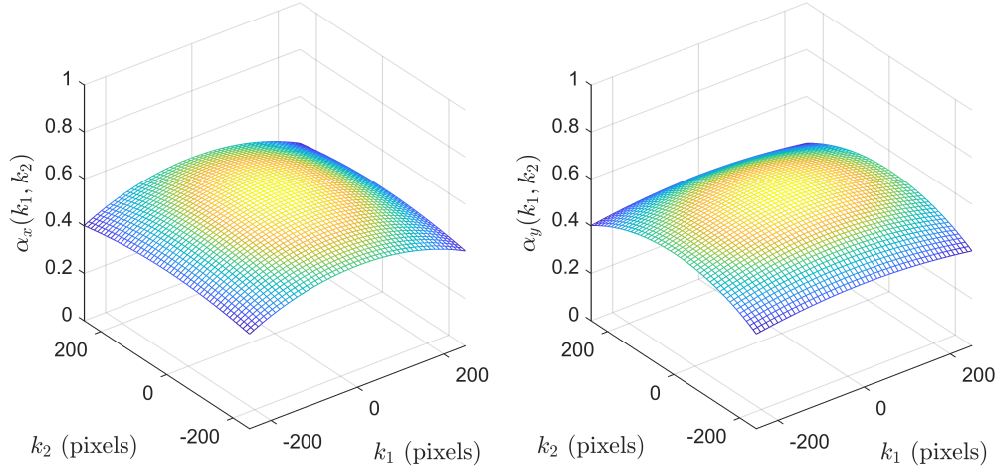


Fig. 10. Global registration tilt correction factors as a function of $\mathbf{k} = [k_1, k_2]^T$ with $M = 250$ (i.e., 501×501 image), $\varepsilon = 0$, and using the optical parameters in Table 1. The x -dimension function is on the left and the y -dimension function is on the right.

This has the Gaussian form

$$G_\alpha(\rho) = \exp\left\{\frac{-\rho^2}{2\sigma_G^2(\alpha)}\right\}, \quad (35)$$

where

$$\sigma_G^2(\alpha) = \frac{r_0^{5/3} D^{1/3}}{6.88(1-\alpha)(\lambda l)^2}. \quad (36)$$

In the spatial domain, Eq. (28) may be expressed as

$$h_\alpha(r) = h_{\text{dif}}(r) * h_{\text{SE}}(r) * g_\alpha(r), \quad (37)$$

where $r = \sqrt{x^2 + y^2}$ is the radial spatial variable. The term $h_{\text{dif}}(r)$ is the inverse Fourier transform of Eq. (29), $h_{\text{SE}}(r)$ is the inverse Fourier transform of Eq. (30), and $g_\alpha(r)$ is a spatial domain Gaussian [2]. This Gaussian is given by

$$g_\alpha(r) = \frac{2\sigma_g^2(\alpha)}{\pi} \exp\left\{-\frac{r^2}{2\sigma_g^2(\alpha)}\right\}, \quad (38)$$

where

$$\sigma_g^2(\alpha) = \frac{1}{4\pi^2\sigma_G^2(\alpha)}. \quad (39)$$

Some example OTFs are shown in Fig. 11 using the optical parameters in Table 1 and $C_n^2(z) = 2.5 \times 10^{-16} \text{ m}^{-2/3}$. The different curves are for different values of M with $\varepsilon = 0$. As M increases, the tilt correction factor decreases for anisoplanatic turbulence. In turn, the residual blurring increases, and the OTF becomes more low-pass in nature. Note that in the limit when $M = 0$ (1×1 block), we have ideal tilt correction with $\alpha = 1$, and the resulting OTF is the average atmospheric short-exposure OTF. On the other extreme, as M approaches infinity, α approaches 0 giving us the long exposure OTF. Also shown in Fig. 11 as dashed lines are the Wiener filter compensated OTFs for $\Gamma = 0.001$. These curves include the Wiener OTF from Eq. (4) as a function of the radial frequency variable ρ . Here the differences in the OTFs are

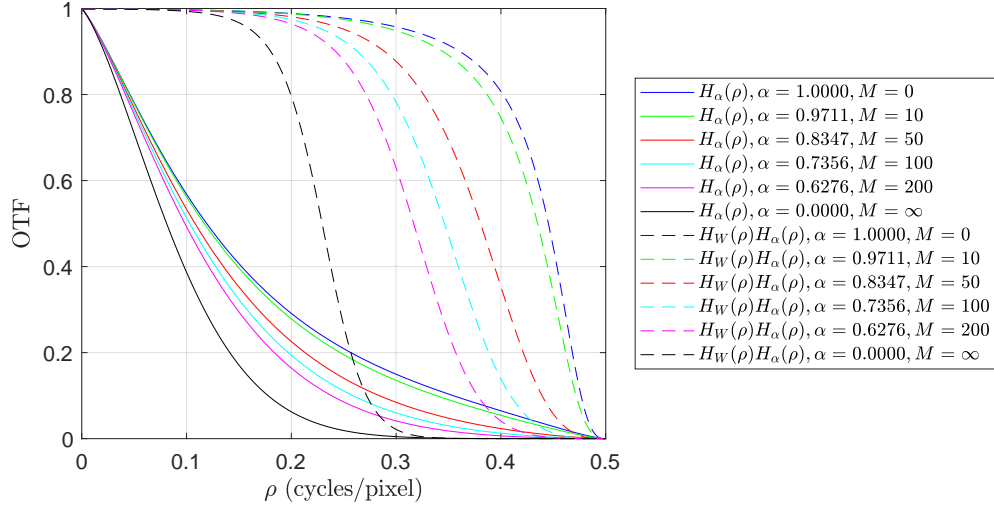


Fig. 11. Overall OTF plots from Eq. (28) for the Optical parameters in Table 1 and $C_n^2(z) = 2.5 \times 10^{-16} \text{ m}^{-2/3}$. Also shown are the OTFs with the Wiener filter from Eq. (4) applied. The different curves are for different patch sizes M assuming $\varepsilon = 0$. As M increases, the tilt correction factor decreases, residual blurring increases, and the OTF becomes more low-pass in nature.

even more pronounced. The OTF curves in Fig. 11 suggest that the smallest M should be used to produce the most tilt correction and the most favorable OTF. However, in practice, as the patch size is decreased the accuracy of the motion estimates declines and requires a higher ε . Thus, registration for OTF improvement requires balancing the patch size M with the motion estimation error ε to create the highest α possible.

5. Spectral Ratio Fried Parameter Estimation

We shall now introduce a modified spectral ratio method for estimating the Fried parameter, r_0 , that can be applied to registered images to address camera motion. This method involves acquiring a sequence of short exposure frames as one would do for image restoration for turbulence mitigation. We will use the short exposure images and also form a long exposure image by averaging the frames. The proposed method involves dividing the spatial-frequency spectrum of long-exposure image by that of the short-exposure images [17]. Based on our model in Section 4, the result should have a Gaussian form. The Fried parameter can be found as a function of the Gaussian variance. One of the novel aspects of the approach presented here lies in how utilize the tilt correction factor to compensate for image registration.

Consider a pristine image spectrum $Z(u, v)$. Acquiring this image with diffraction-limited optics and average short-exposure OTF, we obtain the spectrum

$$Y_1(u, v) = H_1(\rho)Z(u, v) = H_{\text{dif}}(\rho)H_{\text{SE}}(\rho)G_1(\rho)Z(u, v). \quad (40)$$

Note that we are using $\alpha = 1$ because this is assumed to be a true average short-exposure image. Now consider forming a modified long exposure image by averaging the short exposure frames. Let this be given by

$$Y_\alpha(u, v) = H_\alpha(\rho)Z(u, v) = H_{\text{dif}}(\rho)H_{\text{SE}}(\rho)G_\alpha(\rho)Z(u, v). \quad (41)$$

The reason we do not set $\alpha = 0$ is that some registration to compensate for camera motion might be necessary. Compensating for camera motion will also inadvertently compensate for some

turbulence motion. Using the α from Eq. (26) gives us the means to account for this warping tilt reduction as a function of the registration window size. If we form a spectral ratio from Eqs. (41) and (40), we obtain

$$\frac{Y_\alpha(u, v)}{Y_1(u, v)} = \frac{H_\alpha(\rho)Z(u, v)}{H_1(\rho)Z(u, v)} = \frac{H_{\text{dif}}(\rho)H_{\text{SE}}(\rho)G_\alpha(\rho)Z(u, v)}{H_{\text{dif}}(\rho)H_{\text{SE}}(\rho)G_1(\rho)Z(u, v)}. \quad (42)$$

Canceling the like terms and recognizing that $G_1(\rho) = 1$ yields

$$\frac{Y_\alpha(u, v)}{Y_1(u, v)} = \frac{H_\alpha(\rho)}{H_1(\rho)} = G_\alpha(\rho). \quad (43)$$

Thus, the spectral ratio has a Gaussian form given by Eq. (35) with variance $\sigma_G^2(\alpha)$ given by Eq. (36). Let an image-based estimate of this variance be denoted $\hat{\sigma}_G^2$. Finally, using our estimated Gaussian spectral ratio variance in Eq. (36) and solving for r_0 we obtain the Fried parameter estimate

$$\hat{r}_0 = \left[\frac{6.88(\lambda l \hat{\sigma}_G)^2 (1 - \alpha)}{D^{1/3}} \right]^{3/5}. \quad (44)$$

Thus, the problem of r_0 estimation is transformed to that of estimating $\sigma_G^2(\alpha)$ from the spectral ratio function. The parameter α in Eq. (44) gives us the ability to compensate for any camera-motion registration performed.

Example spectra are shown in Fig. 12 to illustrate the Gaussian nature of the spectral ratio. The optical parameters are those in Table 1 and $C_n^2(z) = 2.5 \times 10^{-16} \text{ m}^{-2/3}$. Shown are the diffraction limited OTF, $H_{\text{dif}}(\rho)$, the short-exposure OTF with diffraction, $H_1(\rho)$, the long exposure OTF with diffraction, $H_0(\rho)$, and the ratio that is equal to $G_0(\rho)$. Note that the ratio does have a Gaussian appearance as expressed in Eq. (35). When registration is necessary to compensate for camera motion, the long exposure OTF is replaced with $H_\alpha(\rho)$ and the ratio is given by $G_\alpha(\rho)$ for $\alpha \in (0, 1)$. Note that as α gets larger and approaches 1, the short- and modified long-exposure OTFs converge. This makes estimating the Fried parameter very sensitive to noise and other errors. To prevent this, we recommend using the largest M possible for r_0 estimation. Alternatively, one may use global registration and apply the average α as described in Section 3.4. For restoration purposes, smaller M is desirable, so long as the tilt motion can be estimated accurately. Thus, we propose a two-step process where a large M is first used to compensate for camera motion and estimate r_0 . In a subsequent step, the images would be re-registered using BMA with a relatively small M to provide maximum tilt correction and give the most favorable OTF for the best restoration.

A block diagram of the proposed spectral ratio Fried parameter estimation method is presented in Fig. 13. The process begins with the acquisition of short-exposure frames. If camera motion is present, global registration or BMA registration using the largest practical block size is performed. The registration is important when camera motion is present because we do not want camera motion to produce additional non-turbulence motion blurring that would impact the Fried parameter estimate. At the same time, we want only the minimum turbulence tilt compensation when forming the long exposure image. Unfortunately, by correcting for camera motion, we will invariably also be correcting for some large-scale turbulence warping as well. Turbulence tilt correction is kept to a minimum when we use the largest M possible, as shown in Fig. 8. Global registration offers the best option for correcting camera motion with minimal turbulence tilt correction.

Based on the type of registration, if any, we must generate a corresponding α that represents the level of turbulence tilt correction. If there is no camera motion, no registration is done and we simply set $\alpha = 0$. If BMA registration is used, we set α using Eq. (26) based on the block size governed by M . If global registration is used, we use the α computed according to Section 3.4 based on the full image size.

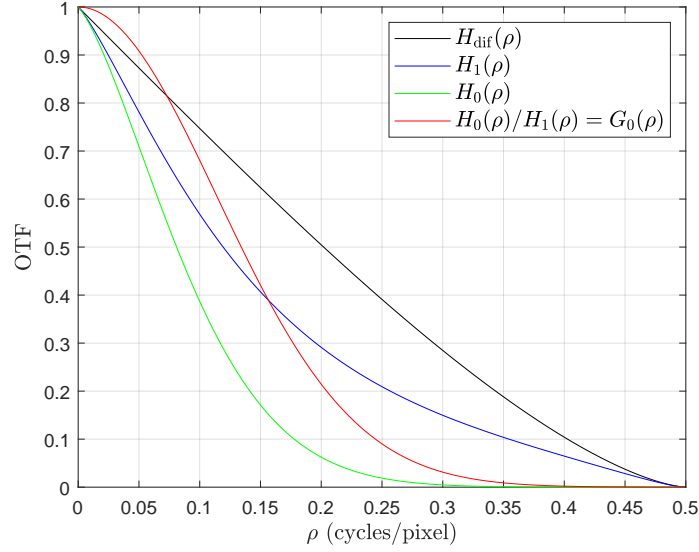


Fig. 12. OTF plots showing the diffraction-limited OTF, short-exposure OTF, long-exposure OTF, and the spectral ratio of the long exposure over the short exposure OTF for the optical parameters in Table 1 and $C_n^2(z) = 2.5 \times 10^{-16} \text{ m}^{-2/3}$. The ratio is a Gaussian and the standard deviation is related to the Fried parameter by Eq. (44).

The registered (or raw) frames are then averaged to form a camera-motion-compensated long-exposure image. Next, the magnitude spatial-frequency spectrum of the long-exposure image is computed. Also, the magnitude spectra of the individual short-exposure frames are computed and averaged. The 2D spectral ratio array is then formed and converted into polar coordinates. A robust estimate of the underlying radial function is formed by computing the median across all angles for each radial distance. Curve fitting is applied to estimate the Gaussian standard deviation $\hat{\sigma}_G$. Finally, Eq. (44) is used to form the estimate \hat{r}_0 . Note that since we have discrete space images, the Fourier transforms are computed using the FFT. Also, windowing with a Tukey window is applied before all FFTs to reduce border discontinuity effects.

A desirable characteristic of the proposed method is that all pixels in the image are utilized in forming the r_0 estimate, adding to robustness. In addition, if image registration is used to address camera motion, the impact of this registration may be accounted for with the tilt correction factor α . As mentioned earlier, this parameter may be determined in the case of constant $C_n^2(z)$ based on optical parameters and the block or image size described by M . Results for specific registration methods can be fine-tuned using the registration error-to-signal ratio parameter ε in Eq. (26). We have obtained excellent results using $\varepsilon = 1/12$ with integer pixel BMA. Note that this is the variance of quantization noise for integer quantization.

One last point to note is that the proposed algorithm assumes a static scene so that the long- and short-exposure images correspond to one another in terms of underlying scene content. In the case of moving objects within the scene, the “movers” will be present in the short-exposure imagery but will be blurred away in the long exposure imagery. This will tend to have the impact of reducing the $\hat{\sigma}_G$ and producing an erroneously low \hat{r}_0 estimate. Thus, it would be helpful to detect scene motion regions [33] and avoid these for r_0 estimation.

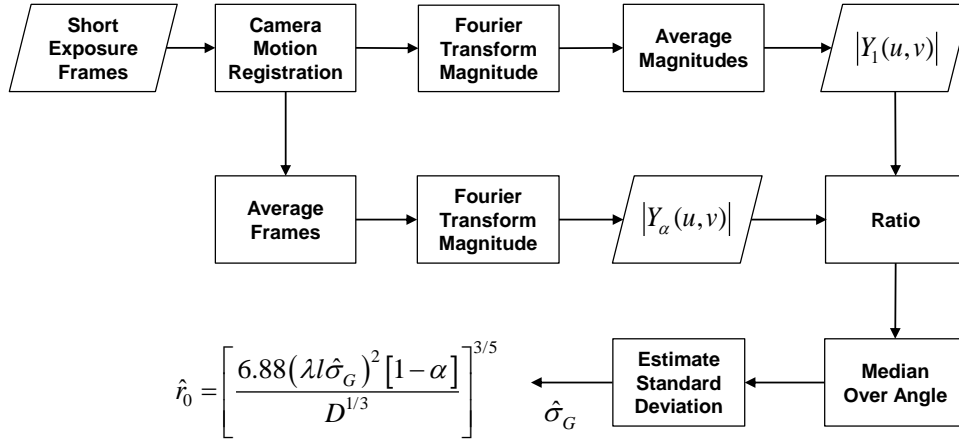


Fig. 13. Block diagram of the proposed spectral ratio Fried parameter estimation method with camera motion registration and compensation using the tilt correction factor α .

6. Experimental Results

In this section we present a number of experimental results to demonstrate the efficacy of the proposed spectral ratio r_0 estimation algorithm presented in Section 5 and turbulence mitigation using the OTF model in Section 4. We first present results using simulated data in Section 6.1 that allow for a detailed quantitative performance analysis. Next, we use real data in Section 6.2.

6.1. Simulated Data

The simulated data are generated using the numerical wave-propagation tool developed by Hardie *et al* [22]. This simulator produces realistic anisoplanatic turbulence degradations and it has been validated using a number of key turbulence statistics [22]. We use the optical parameters in Table 1 and the turbulence parameters listed in Table 2. The detailed simulator parameters match those in the original simulator paper [22]. All of the simulated frames are derived from the truth images shown in Fig. 14. These are standard publicly available 8-bit grayscale images sized to 501×501 pixels. As can be seen in Table 2, we model 6 turbulence levels with constant $C_n^2(z)$ profiles. For each truth image and each turbulence level, 300 temporally independent frames are generated. Additive Gaussian noise is included with a standard deviation of 1 digital unit. Table 2 shows several statistics for each turbulence level.

6.1.1. Fried Parameter Estimation with Simulated Data

For each turbulence level, we use several variations of our spectral ratio method to estimate the Fried parameter. The results are reported in Table 3 for the Boats image and Table 4 for Stream and Bridge. The results for Boats are also plotted in Fig. 15 for the reader's convenience. The percent errors for the various estimates compared with the true r_0 are also shown in the tables.

The estimates labeled "Stationary" use no registration and would be appropriate for a stationary camera. Since there is no camera motion, we use $\alpha = 0$, as there is no tilt correction taking place by means of registration. This method of estimating r_0 has a maximum absolute percent error of 5.34% for the datasets used. Now consider the case of using global registration to compensate for possible camera motion. If this is done without applying an appropriate tilt correction factor, the r_0 estimate is significantly inflated. This is because the camera registration compensates for turbulence motion, making the turbulence seem weaker, giving rise to a high Fried parameter estimate. This effect can be seen clearly in Fig. 15 for for the curve labeled "Global ($\alpha = 0$)".

Table 2. Turbulence parameters for 6 levels of turbulence generated with the anisoplanatic turbulence simulator [22] to test the spectral ratio r_0 estimator. The patch and residual tilt variance values are for $M = 100$ (201×201 pixel patch).

Parameter	Turbulence Degradation					
	Level 1	Level 2	Level 3	Level 4	Level 5	Level 6
$C_n^2 \times 10^{-15}$ ($\text{m}^{-2/3}$)	0.1000	0.2500	0.5000	1.0000	1.5000	2.0000
Theoretical r_0 (m)	0.1901	0.1097	0.0724	0.0478	0.0374	0.0315
Theoretical D/r_0 (unitless)	1.0697	1.8536	2.8096	4.2585	5.4314	6.4547
Isoplanatic Angle (pixels)	6.6174	3.8188	2.5194	1.6622	1.3033	1.0966
RMS Tilt (pixels)	0.9026	1.4272	2.0183	2.8543	3.4958	4.0367
Tilt Variance (pixels ²)	0.8147	2.0368	4.0736	8.1473	12.2209	16.2946
Patch Tilt Variance (pixels ²)	0.5333	1.3333	2.6666	5.3333	7.9999	10.6666
Residual Tilt Variance (pixels ²)	0.2154	0.5385	1.0770	2.1541	3.2311	4.3082



(a)



(b)

Fig. 14. Standard publicly available truth images used for simulation results. The images are converted to grayscale and resized to a pixel size of 501×501 . (a) Boats [34], (b) Stream and Bridge [35].

However, by computing and applying the global tilt correction factor, as described in Section 3.4, excellent results are achieved. This can be seen in Fig. 15 for for the curve labeled “Global ($\alpha = 0.5252$)”. This method has a maximum absolute percent error of 5.71% for the datasets used.

The remaining estimates are formed using BMA registration with $M = 100$ (201×201 patch size). As expected, the uncompensated BMA estimate (i.e., $\alpha = 0$) is too large. Interestingly, using the α as computed in Eq. (26) with $\varepsilon = 0$, we get an underestimate of the Fried parameter. This is due to the fact that BMA registration is imperfect and is computed here only to the nearest whole pixel. Thus, it is achieving less tilt correction than a theoretically ideal patch registration

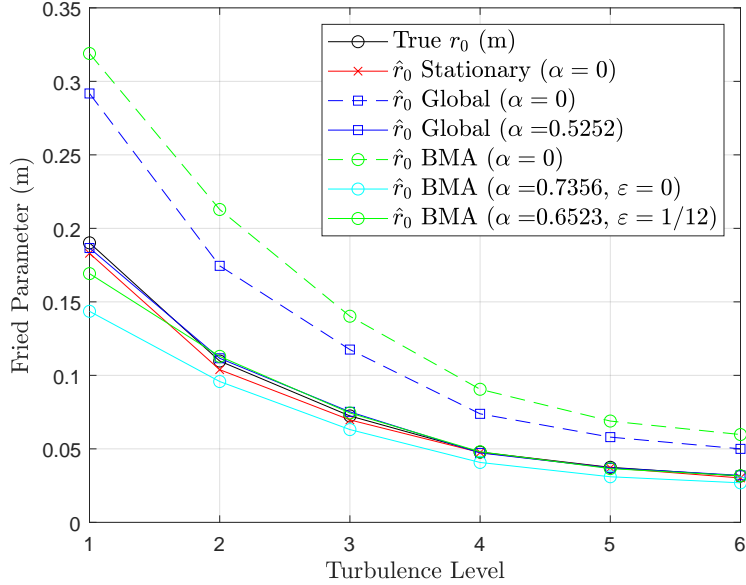


Fig. 15. Spectral ratio Fried parameter estimates for the 6 levels of turbulence in Table 2 and the image Boats.

of that size. By setting the registration error-to-signal value to be $\varepsilon = 1/12$, this effect can be largely compensated for, as shown in Fig. 15.

It should be noted that the global registration is a more practical method for compensating for camera motion. It can be done with subpixel accuracy very efficiently. We employ a normalized cross-correlation to get to the nearest whole pixel, and then follow this with the iterative gradient method of Lucas and Kanade [36] for subpixel accuracy. Because this global registration is very accurate, we use $\varepsilon = 0$. The larger effective block size of global registration also allows for less turbulent tilt correction (i.e., smaller α), and this generally helps to improve the r_0 estimate. In contrast, BMA with large block sizes is very computationally demanding, especially if one seeks subpixel accuracy. The maximum block size with BMA is also more limited because of border effects.

To better understand the impact of registration on the Fried parameter estimation process, consider the images shown in Fig. 16. These images show a region of interest for the Boats data with level 4 turbulence. The truth image is shown in Fig. 16(a) and a single short exposure image is shown in Fig. 16(b). The 300 frame average with no camera motion or registration is shown in Fig. 16(c). Clearly this long exposure image is much more blurred than the short exposure image. The relationship between the long and short exposure images is what allows us to estimate r_0 . When camera motion is present, global registration is required. The average of the globally registered frames is shown in Fig. 16(d). Note that there is less blurring in Fig. 16(d) than in Fig. 16(c) due to the registration. This reduction in blurring is what leads to the inflated r_0 estimate, if left uncompensated.

Spectral ratios and the Gaussian fitting curves for the same data are shown in Fig. 17 as a function of spatial frequency in units of cycles per pixel spacing. Figure 17(a) shows the spectral ratio radial function for the case of a stationary camera and no registration. Here, the long exposure image has a low cut-off frequency, and the spectral ratio has a small σ_G . In Fig. 17(c), the spectral ratio is shown where BMA registration with $M = 100$ is applied for camera motion compensation. The modified long exposure image is now less blurred, and this leads to a larger

Table 3. Spectral ratio Fried parameter estimation error analysis for the 6 levels of turbulence detailed in Table 2 and the truth image Boats.

Parameter	Turbulence Degradation					
	Level 1	Level 2	Level 3	Level 4	Level 5	Level 6
Theoretical r_0 (m)	0.1901	0.1097	0.0724	0.0478	0.0374	0.0315
Stationary \hat{r}_0 (m)	0.1830	0.1039	0.0697	0.0475	0.0371	0.0302
Percent Error	-3.75%	-5.34%	-3.73%	-0.46%	-1.01%	-4.17%
Global \hat{r}_0 (m) ($\alpha = 0$)	0.2913	0.1738	0.1168	0.0734	0.0575	0.0495
Percent Error	53.20%	58.37%	61.40%	53.66%	53.66%	57.23%
Global \hat{r}_0 (m) ($\alpha = 0.5252$)	0.1863	0.1112	0.0747	0.0469	0.0368	0.0317
Percent Error	-2.01%	1.30%	3.24%	-1.72%	-1.71%	0.57%
BMA \hat{r}_0 (m) ($\alpha = 0$)	0.3189	0.2128	0.1402	0.0905	0.0689	0.0597
Percent Error	67.74%	93.96%	93.69%	89.55%	84.04%	89.56%
BMA \hat{r}_0 (m) ($\varepsilon = 0$)	0.1436	0.0958	0.0631	0.0408	0.0310	0.0269
Percent Error	-24.50%	-12.69%	-12.81%	-14.68%	-17.16%	-14.67%
BMA \hat{r}_0 (m) ($\varepsilon = 1/12$)	0.1692	0.1129	0.0744	0.0480	0.0366	0.0317
Percent Error	-11.01%	2.91%	2.77%	0.57%	-2.35%	0.57%

Table 4. Spectral ratio Fried parameter estimation error analysis for the 6 levels of turbulence detailed in Table 2 and the truth image Stream and Bridge.

Parameter	Turbulence Degradation					
	Level 1	Level 2	Level 3	Level 4	Level 5	Level 6
Theoretical r_0 (m)	0.1901	0.1097	0.0724	0.0478	0.0374	0.0315
Stationary \hat{r}_0 (m)	0.1823	0.1058	0.0692	0.0473	0.0371	0.0298
Percent Error	-4.15%	-3.56%	-4.41%	-0.99%	-1.00%	-5.33%
Global \hat{r}_0 (m) ($\alpha = 0$)	0.2803	0.1684	0.1121	0.0716	0.0556	0.0466
Percent Error	47.41%	53.50%	54.80%	49.94%	48.42%	47.80%
Global \hat{r}_0 (m) ($\alpha = 0.5252$)	0.1793	0.1077	0.0717	0.0458	0.0356	0.0298
Percent Error	-5.71%	-1.81%	-0.98%	-4.10%	-5.07%	-5.46%
BMA \hat{r}_0 (m) ($\alpha = 0$)	0.3096	0.2071	0.1415	0.0899	0.0663	0.0565
Percent Error	62.81%	88.71%	95.41%	88.24%	77.13%	79.42%
BMA \hat{r}_0 (m) ($\varepsilon = 0$)	0.1394	0.0932	0.0637	0.0405	0.0299	0.0254
Percent Error	-26.71%	-15.05%	-12.04%	-15.27%	-20.27%	-19.24%
BMA \hat{r}_0 (m) ($\varepsilon = 1/12$)	0.1643	0.1099	0.0751	0.0477	0.0352	0.0300
Percent Error	-13.62%	0.12%	3.68%	-0.13%	-6.02%	-4.81%

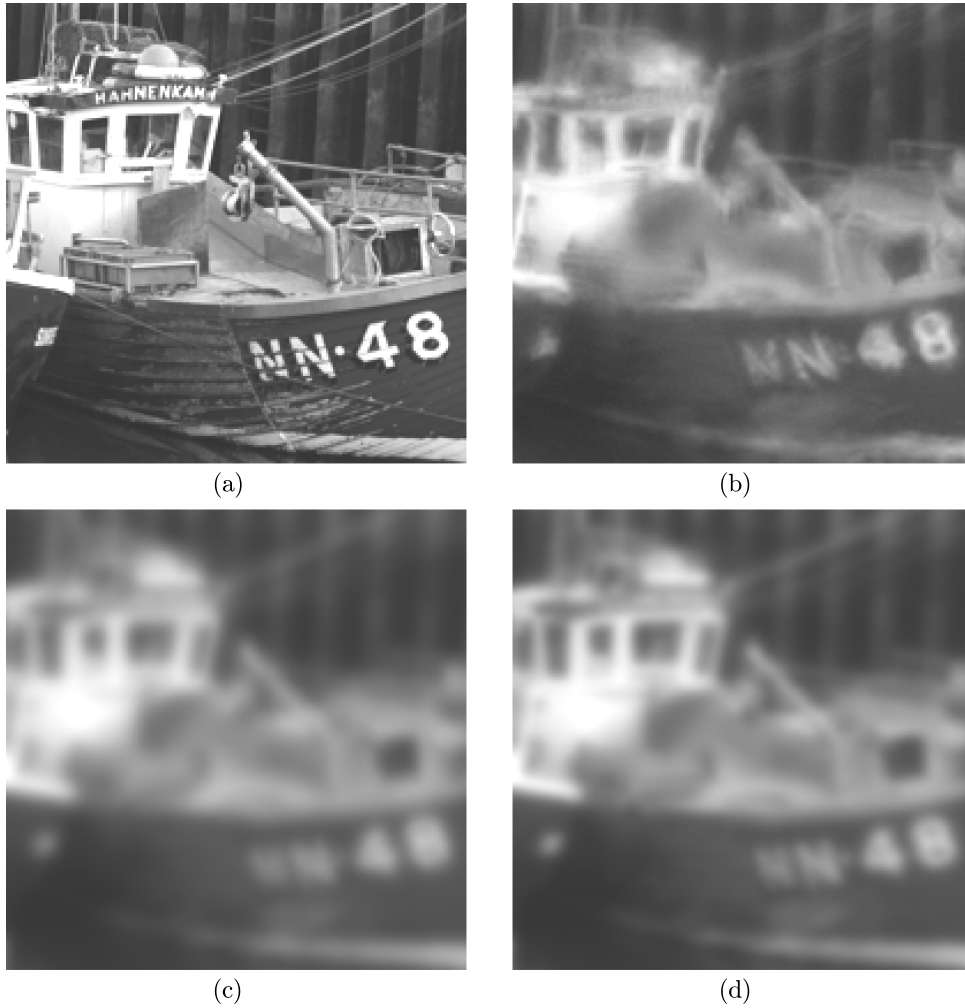


Fig. 16. Region of interest images for level 4 turbulence from Table 2 for the image Boats. (a) Truth image, (b) Frame 1 short-exposure image, (c) long-exposure image with no camera motion, (d) motion compensated frame average using global registration.

σ_G . Finally in Fig. 17(e), we see the spectral ratio for global registration. Here σ_G is smaller than with BMA, but still larger than with no registration. By using the appropriate α for each scenario, all of these can lead to effective r_0 estimates.

6.1.2. Turbulence Mitigation with Simulated Data

In this section we examine turbulence mitigation using the OTF model in Section 4 with the α defined in Section 3.2 and the spectral ratio r_0 estimate from Section 5. Performance is measured in terms of peak signal-to-noise ratio (PSNR) and the structural similarity index (SSIM) [37]. In both cases, a larger number represents a better restoration. In all cases the r_0 used for these restorations comes from the spectral ratio estimate assuming camera motion and global registration, as listed in Tables 3 and 4. The α employed is based on the type of registration. For global registration results we use the average value of $\alpha = 0.5252$ that corresponds to the full image size of $M = 250$. For BMA, we use $M = 10$ and a corresponding value of $\alpha = 0.8878$. This α is computed using $\varepsilon = 1/12$. The Wiener filter NSR used is $\Gamma = 0.001$.

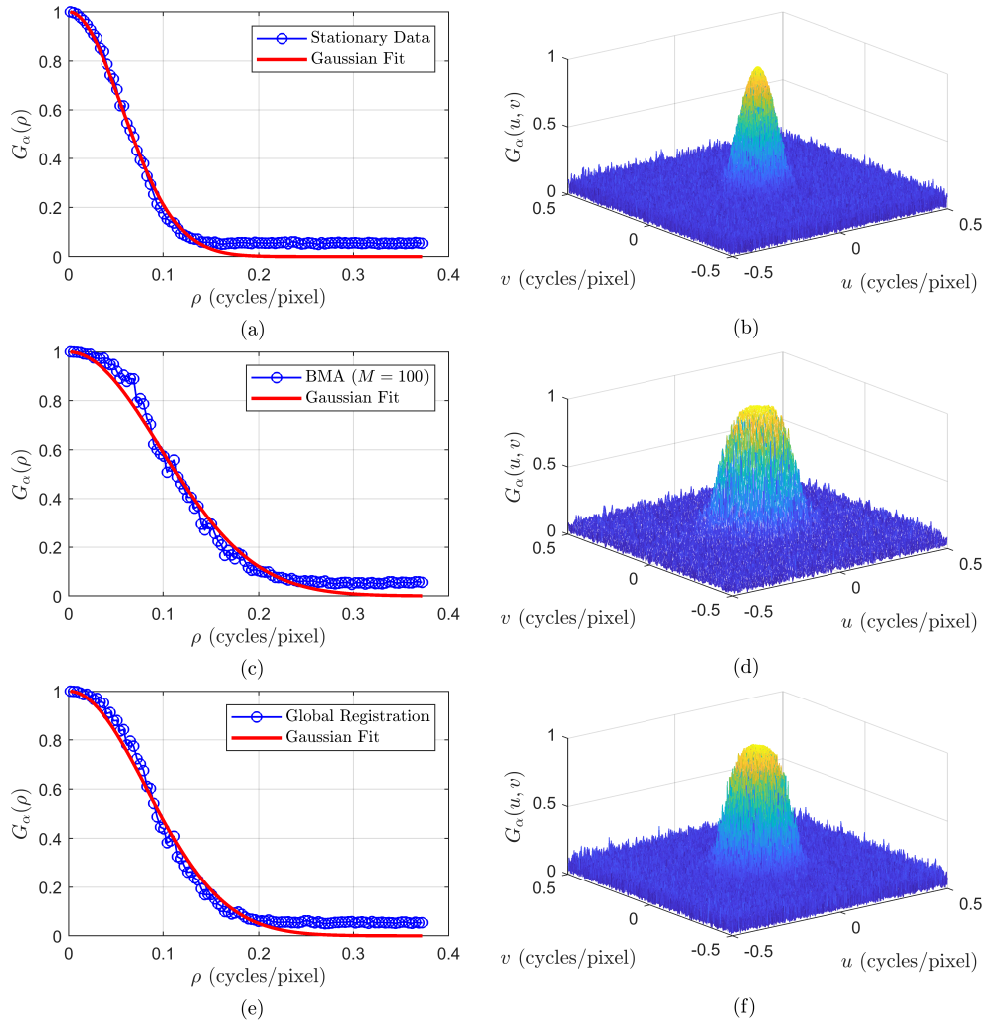


Fig. 17. Spectral ratio Gaussian fitting for level 4 turbulence defined in Table 2 for the image Boats. Stationary camera data with no registration is shown in (a) and (b). Data for BMA registered frames using $M = 100$ are shown in (c) and (d). Data for global registration are shown in (e) and (f).

The PSNR results for the two truth images are provided in Tables 5 and 6, respectively. The SSIM results are shown in Tables 7 and 8. The PSNR and SSIM results for the Boats image data are plotted in Fig. 18 and 19, respectively. These results show that employing registration prior to averaging and Wiener filtering boosts performance. Here BMA with $M = 10$ is better than global registration because the increased tilt correction produces an image with less blurring for the Wiener filter to restore.

Image results for turbulence mitigation are shown in Fig. 20 for the Boats image data. The truth region of interest is shown in Fig. 20(a). The average frame (i.e., long exposure) with Wiener filter applied is shown in Fig. 20(b). The average of the globally registered frames with Wiener filter applied is shown in Fig. 20(c). Finally, the average of $M = 10$ BMA registered frames with Wiener filter applied is shown in Fig. 20(d). Note that the best restored image detail is seen in Fig. 20(d), followed by Figs. 20(c) and (b). The more comprehensive the registration, the less blurred the input is to the Wiener filter, and the better the final result.

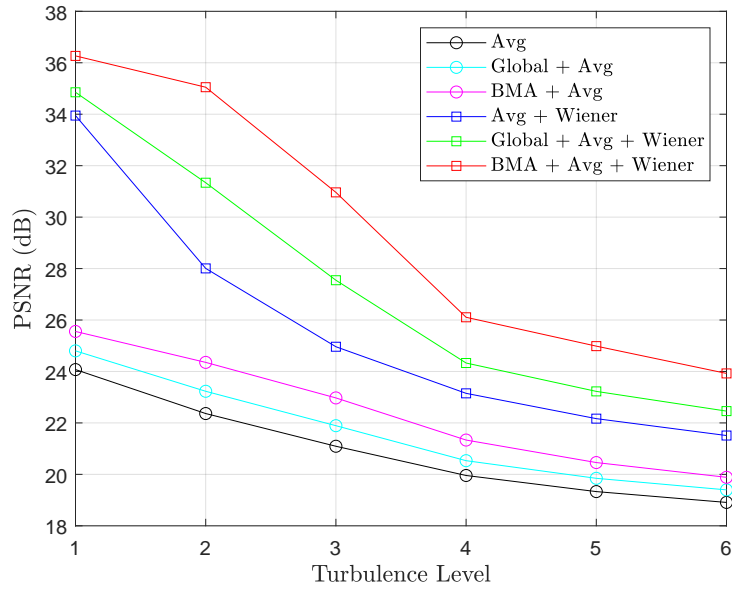


Fig. 18. Turbulence mitigation quantitative error analysis using the PSNR (dB) metric for the 6 turbulence levels in Table 2 using the image Boats. The r_0 value used is from the global registration spectral ratio estimate for this image sequence.

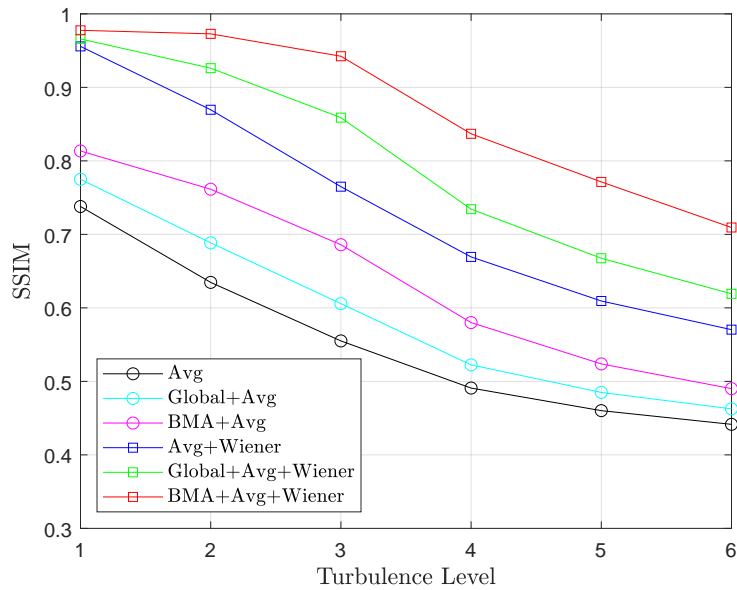


Fig. 19. Turbulence mitigation quantitative error analysis using the SSIM metric for the 6 turbulence levels in Table 2 using the image Boats. The r_0 value used is from the global registration spectral ratio estimate for this image sequence.

Table 5. Turbulence mitigation PSNR (dB) results for the Boats image using the optical parameters in Table 1 and the 6 turbulence levels in Table 2. The r_0 value used is from the global registration spectral ratio estimate for this image sequence.

Turbulence Mitigation Method	Turbulence Degradation					
	Level 1	Level 2	Level 3	Level 4	Level 5	Level 6
Frame 1	22.8144	21.0166	19.5873	19.4271	19.3396	17.1386
Avg	24.0733	22.3642	21.0926	19.9563	19.3304	18.9094
Global + Avg	24.8010	23.2296	21.8923	20.5321	19.8463	19.3972
BMA ($M = 10$) + Avg	25.5550	24.3532	22.9716	21.3339	20.4592	19.8855
Avg + Wiener	33.9471	28.0064	24.9611	23.1497	22.1659	21.5099
Global + Avg + Wiener	34.8527	31.3373	27.5469	24.3288	23.2257	22.4591
BMA ($M = 10$) + Avg + Wiener	36.2669	35.0499	30.9621	26.1062	24.9845	23.9241

Table 6. Turbulence mitigation PSNR (dB) results for the Stream and Bridge image using the optical parameters in Table 1 and the 6 turbulence levels in Table 2. The r_0 value used is from the global registration spectral ratio estimate for this image sequence.

Turbulence Mitigation Method	Turbulence Degradation					
	Level 1	Level 2	Level 3	Level 4	Level 5	Level 6
Frame 1	23.1948	22.0832	19.5952	20.0127	20.2346	17.5237
Avg	24.1645	22.7428	21.6037	20.5968	20.0119	19.5737
Global + Avg	24.7622	23.4439	22.2945	21.1216	20.4964	20.0397
BMA ($M = 10$) + Avg	25.4163	24.4391	23.2534	21.8289	21.0319	20.4842
Avg + Wiener	31.2960	27.0460	24.7814	23.1652	22.3452	21.8384
Global + Avg + Wiener	32.3660	29.2104	26.4898	24.0227	23.0100	22.3299
BMA ($M = 10$) + Avg + Wiener	33.5384	32.3853	28.8911	25.5475	24.2221	23.1938

6.2. Real Camera Data

While we believe the simulated results are compelling, we believe it is also important to provide results for real sensor data. These results come from a camera with the specifications listed in Table 9. An image sequence containing 600 frames is acquired from a stationary camera imaging a trailer and test pattern at a range of 1.8701 km. The image data are cropped to a size of 1001×1001 for subsequent processing. An example image is shown in the results presented in Section 6.2.2.

6.2.1. Fried Parameter Estimation with Real Camera Data

Our first experiment with the real data involves Fried parameter estimation. The spectral ratio data for the stationary camera and no registration are shown in Fig. 21. These appear to be very similar to what we have observed with the simulated data. From the spectral ratio and using $\alpha = 0$,

Table 7. Turbulence mitigation SSIM results for the Boats image using the optical parameters in Table 1 and the 6 turbulence levels in Table 2. The r_0 value used is from the global registration spectral ratio estimate for this image sequence.

Turbulence Mitigation Method	Turbulence Degradation					
	Level 1	Level 2	Level 3	Level 4	Level 5	Level 6
Frame 1	0.6965	0.6269	0.5259	0.5001	0.5003	0.4328
Avg	0.7379	0.6347	0.5550	0.4909	0.4602	0.4415
Global + Avg	0.7749	0.6885	0.6058	0.5225	0.4850	0.4626
BMA ($M = 10$) + Avg	0.8134	0.7614	0.6859	0.5800	0.5238	0.4901
Avg + Wiener	0.9557	0.8695	0.7649	0.6693	0.6094	0.5704
Global + Avg + Wiener	0.9659	0.9261	0.8588	0.7343	0.6675	0.6191
BMA ($M = 10$) + Avg + Wiener	0.9776	0.9728	0.9424	0.8368	0.7714	0.7093

Table 8. Turbulence mitigation SSIM results for the Stream and Bridge image using the optical parameters in Table 1 and the 6 turbulence levels in Table 2. The r_0 value used is from the global registration spectral ratio estimate for this image sequence.

Turbulence Mitigation Method	Turbulence Degradation					
	Level 1	Level 2	Level 3	Level 4	Level 5	Level 6
Frame 1	0.6142	0.5320	0.4143	0.3962	0.3940	0.3323
Avg	0.6470	0.5318	0.4452	0.3831	0.3547	0.3379
Global + Avg	0.6896	0.5896	0.4983	0.4130	0.3778	0.3562
BMA ($M = 10$) + Avg	0.7373	0.6774	0.5916	0.4746	0.4151	0.3811
Avg + Wiener	0.9330	0.8214	0.6909	0.5811	0.5107	0.4734
Global + Avg + Wiener	0.9473	0.8918	0.8023	0.6460	0.5637	0.5120
BMA ($M = 10$) + Avg + Wiener	0.9597	0.9536	0.9065	0.7768	0.6794	0.5889

we obtain the “Stationary” r_0 estimates plotted in Fig. 22. A single 600 frame r_0 estimate is shown along with a temporal sequence of estimates using a 201 frame temporal moving window. For reference, the r_0 measurement provided by the MZA Associates Delta System [12] is shown. The nearest temporal MZA value for r_0 is 0.031 m, and the Stationary spectral ratio estimate is 0.0302 m. This represents only a -2.61% difference, which is in keeping with the errors seen using the simulated data.

When global registration is applied to the acquired frames to emulate what would be required with camera motion, we obtain a different set of results. For these results we compute the global registration average tilt correction factor for $M = 500$ yielding $\alpha = 0.5077$. The corresponding r_0 estimates are shown in Fig. 22 as “Global” estimates. Both a 600 frame estimate and sequence of 201 frame moving window results are shown. The 600 frame global registration estimate is 0.0266 m. This represents a -14.32% difference from the MZA value. We believe this increased error here may be largely the result of a highly variable $C_n^2(z)$ profile. Estimated MZA profile

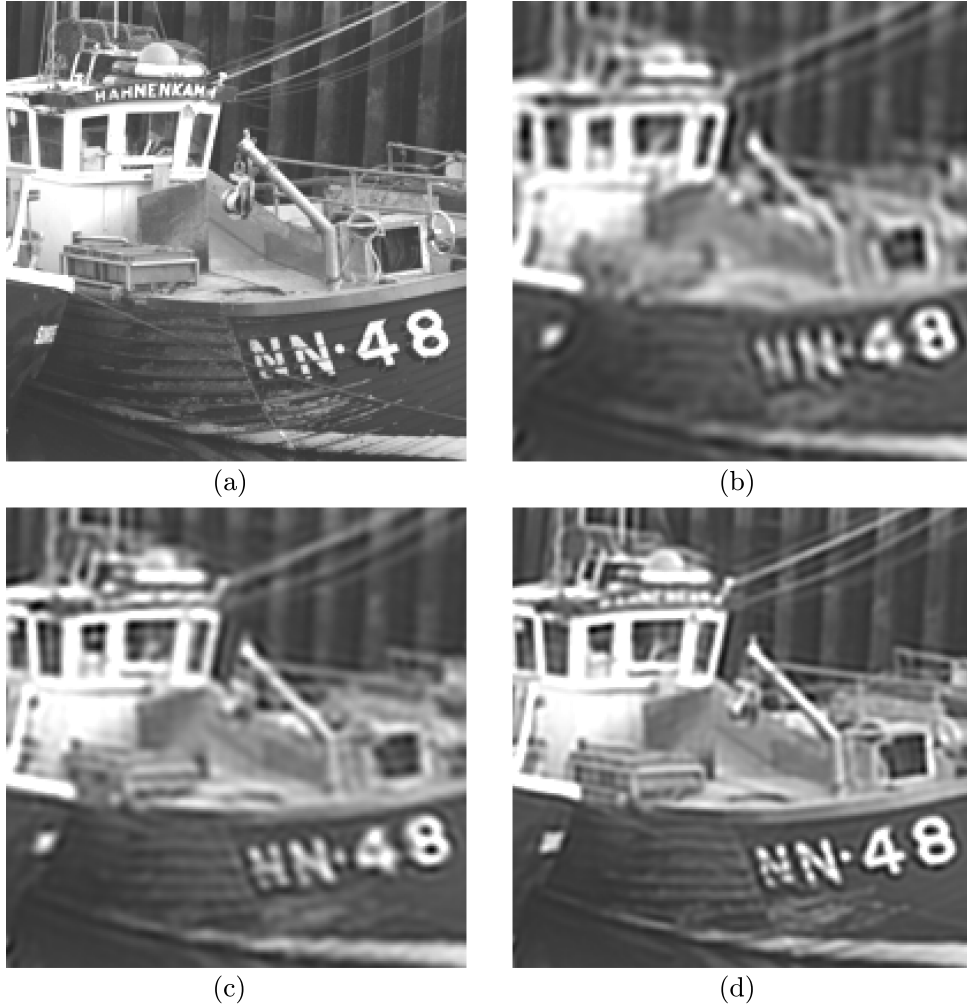


Fig. 20. Turbulence mitigation image results for level 4 turbulence from Table 2 with the image Boats. Regions of interest are shown for: (a) truth, (b) average + Wiener, (c) global registration + average + Wiener, (d) BMA ($M = 10$) + average + Wiener.

data suggests that there is heavier turbulence close to the object. As shown in Fig. 9, a constant path assumption leads to an inflated α in this scenario. In turn, this leads to an underestimate of r_0 based on Eq. (44). Even with this effect, the global registration based r_0 estimate may still be accurate enough for many applications. Note that the stationary r_0 estimate is not adversely impacted by $C_n^2(z)$ profile variation in this way because no tilt correction factor is needed in that case.

6.2.2. Turbulence Mitigation with Real Camera Data

Turbulence mitigation image results using the real camera data are shown in Fig. 23. A single short exposure frame is shown in Fig. 23(a). The 600 frame temporal average is shown in Fig. 23(b). Zoomed-in regions for these two images are shown in Figs. 23(c) and (d), respectively. The average frame with Wiener filter is shown in Fig. 23(e). The output of the Wiener filter operating on the average of BMA ($M = 15$) registered frames is shown in Fig. 23(f). The stationary spectral ratio estimate of $\hat{r}_0 = 0.0302$ m is used. For the result in Fig. 23(e), we use

Table 9. Optical parameters for the real camera data.

Parameter	Value
Aperture	$D = 0.1333$ m
Focal length	$l = 3.7320$ m
F-number	$f/\# = 28$
Wavelength	$\lambda = 0.5500$ μm
Object distance	$L = 1870.1$ m
Actual pixel spacing (focal plane)	$\delta = 6.4500$ μm

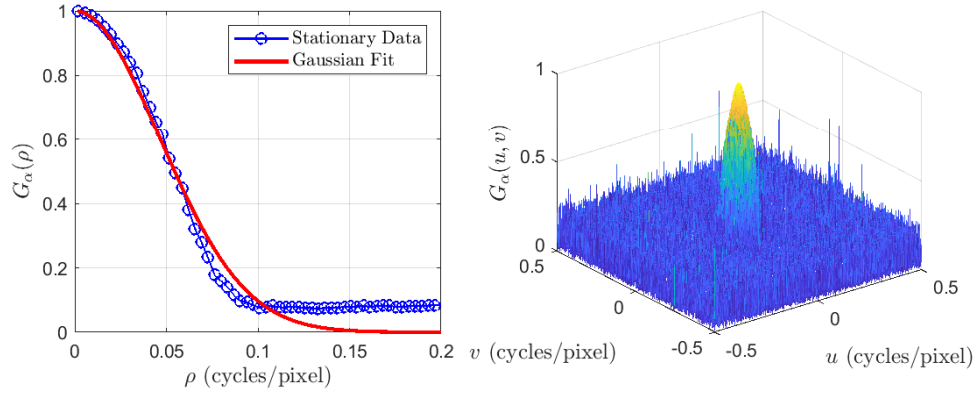


Fig. 21. Spectral ratio data for the 600 frames real camera image sequence. Radial data with Gaussian curve fitting is shown on the left. The 2D spectral ratio data is shown on the right.

$\alpha = 0$. For the result in Fig. 23(f) we use the calculated value of $\alpha = 0.8958$ that corresponds to $M = 15$ and $\varepsilon = 1/12$. Note the improvement in Fig. 23(f) using BMA registration over the result in Fig. 23(e). By including registration the restored image appears sharper and appears to have less noise. The extra noise reduction is from fixed pattern noise attenuation that results from averaging shifted frames [38].

7. Conclusions

In this paper, we have presented turbulence tilt correlation statistics for two point sources as a function of the parallel and perpendicular separation distances. We converted these into 2D WSS autocorrelation functions characterizing the random 2D tilt fields from turbulence. We believe these help to inform a variety turbulence modeling and mitigation applications. One way these statistics can be helpful is in understanding and modeling the impact of various image registration methods. We are able to model the residual tilt variance in the case of patch based image registration such as BMA and global image registration. We model these registration operations as LSI filters applied to the random tilt fields. The output random process has reduced tilt variance. We define the tilt correction factor as one minus the ratio of the residual tilt variance to total input tilt variance. We have shown that this tilt correction factor is only a function of

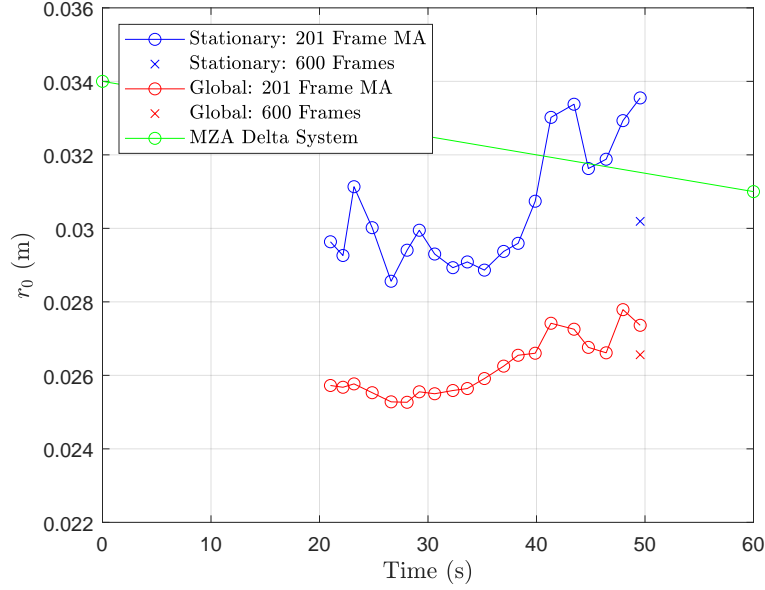


Fig. 22. Fried parameter estimation using the real camera image sequence. “Stationary” results are with no camera motion and no registration. “Global” results are using global image registration. Ground truth is provided by the MZA Delta System.

the optical parameters and block size M for a constant $C_n^2(z)$ path. This gives us the ability to understand and quantify how effective image registration will be for different patch or image sizes defined by M , independent from the potentially unknown level of turbulence.

We use the tilt correction factor to model an atmospheric OTF that includes the impact of image registration. This OTF model is then used to develop a modified spectral ratio Fried parameter estimation algorithm that can accommodate camera motion. Our method for Fried parameter estimation uses all of the pixels in the acquired images and does not require specialized sources or target images. With the ability to estimate the Fried parameter and determine the tilt correction factor, a complete OTF model can be defined and used for turbulence mitigation.

The experimental results with simulated data show quantitatively that the Fried parameter estimation is very accurate over a wide range of turbulence levels on the datasets studied. Results with real data in the stationary camera case are in good agreement with measured ground truth. When registration is employed, higher errors were observed, and this is likely due to a non-constant $C_n^2(z)$ profile. The goal of image registration here is to correct for camera motion with the least impact on the turbulence and the smallest tilt correction factor possible. We have found that global registration can be used to compensate for camera motion and still preserve enough turbulence information to be able to effectively estimate r_0 , provided the appropriate tilt correction parameter is employed.

For BMWF turbulence mitigation, we have shown that our OTF model with estimated r_0 and tilt correction factor is highly effective. We believe the quantitative results with simulated data, and the real camera data results, support this conclusion. In this application, the goal of image registration is to perform the most atmospheric tilt correction possible. A high level of tilt correction produces a fused image with less turbulence motion blurring as the starting point for the Wiener filter restoration. This is achieved by employing a BMA registration algorithm with a relatively small M . When too small an M is used, registration errors limit performance. If too large an M is used, less tilt correction is achieved. Thus, a balance must be achieved between

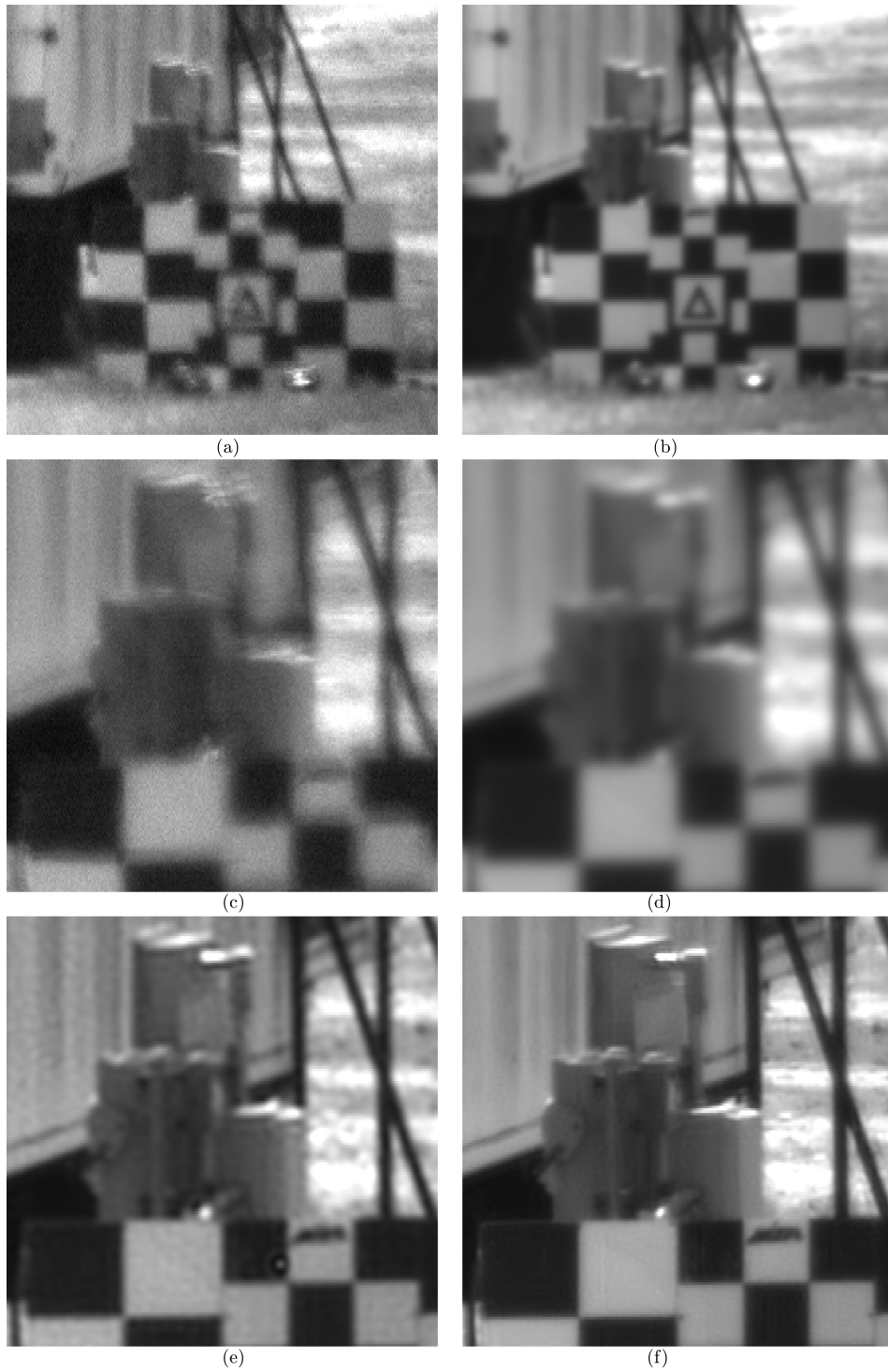


Fig. 23. Turbulence mitigation image results for the real camera data. (a) Short exposure Frame 1, (b) 600 frame average, (c) region of interest for short exposure Frame 1, (d) region of interest for the 600 frame average, (e) average + Wiener filter, (f) BMA ($M = 15$) + average + Wiener filter.

these two factors.

Funding

This work has been supported in part under AFRL Award No. FA8650-17-D-1801. Approved for public release under case number AFRL-2020-0563.

Acknowledgments

The authors would like to thank Dr. Barry Karch at AFRL for supporting this project and providing technical feedback. Thanks to Joe French at Leidos for technical feedback and project management support. We also thank Bruce Wilcoxon, Amanda Caplinger, and Julie Tollefson with Leidos for project management support. Thank you to the engineering teams at Leios and MZA Associates for their roles in acquiring the real data used here. Thanks to Yakov Diskin at MZA Associates for kindly providing information related to their Delta system for atmospheric characterization.

Disclosures

The authors declare no conflicts of interest.

Data availability

The truth images used here may be obtained in [34,35]. The data with turbulence were simulated using the method in [22]. The real camera data are not publicly available at this time.

References

1. M. C. Roggemann and B. M. Welsh, *Imaging through Turbulence*, Laser and Optical Science and Technology (CRC Press, 1996).
2. R. C. Hardie, M. A. Rucci, A. J. Dapone, and B. K. Karch, "Block matching and Wiener filtering approach to optical turbulence mitigation and its application to simulated and real imagery with quantitative error analysis," *Opt. Eng.* **56**, 1 – 16 (2017).
3. R. C. Hardie, M. Rucci, B. K. Karch, A. J. Dapone, D. R. Droegge, and J. C. French, "Fusion of interpolated frames superresolution in the presence of atmospheric optical turbulence," *Opt. Eng.* **58**, 1 – 16 (2019).
4. B. K. Karch and R. C. Hardie, "Robust super-resolution by fusion of interpolated frames for color and grayscale images," *Front. Phys.* **3**, 28 (2015).
5. D. L. Fried, "Optical resolution through a randomly inhomogeneous medium for very long and very short exposures," *J. Opt. Soc. Am.* **56** (1966).
6. L. Sjöqvist, M. Henriksson, and O. Steinvall, "Simulation of laser beam propagation over land and sea using phase screens: a comparison with experimental data," in *Proc. SPIE 5989*, (2005), pp. 123 – 134.
7. X. Wang and Y. Song, "Transmission characteristics of Bessel–Gaussian vortex beams propagating along both longitudinal and transverse directions in a subway tunnel," *Opt. Eng.* **57**, 1 – 9 (2018).
8. M. R. Chatterjee, A. Mohamed, and F. S. Almeahadi, "Secure free-space communication, turbulence mitigation, and other applications using acousto-optic chaos," *Appl. Opt.* **57**, C1–C13 (2018).
9. S. R. Bose-Pillai, J. E. McCrae, C. A. Rice, R. A. Wood, C. E. Murphy, and S. T. Fiorino, "Estimation of atmospheric turbulence using differential motion of extended features in time-lapse imagery," *Opt. Eng.* **57**, 1 – 12 (2018).
10. A. Mohamed and M. R. Chatterjee, "Non-chaotic and chaotic propagation of stationary and dynamic images through MVKS turbulence," *J. Mod. Opt.* **66**, 1392–1407 (2019).
11. M. Sarazin and F. Roddier, "The ESO differential image motion monitor," *Astron. Astrophys.* **227**, 294–300 (1990).
12. "DELTA Imaging Path Turbulence Monitor, PM-02-600," Available at <https://www.mza.com/>.
13. S. Gladysz, M. Segel, C. Eisele, R. Barros, and E. Sucher, "Estimation of turbulence strength, anisotropy, outer scale and spectral slope from an LED array," in *Laser Communication and Propagation through the Atmosphere and Oceans IV*, vol. 9614 A. M. J. van Eijk, C. C. Davis, and S. M. Hammel, eds., International Society for Optics and Photonics (SPIE, 2015), pp. 1 – 7.
14. S. Zamek and Y. Yitzhaky, "Turbulence strength estimation from an arbitrary set of atmospherically degraded images," *J. Opt. Soc. Am. A* **23**, 3106–3113 (2006).
15. S. Gladysz, R. B. Galle, R. L. Johnson, and L. Kann, "Image reconstruction of extended objects: demonstration with the Starfire Optical Range 3.5m telescope," in *Optics in Atmospheric Propagation and Adaptive Systems XV*, vol. 8535 K. Stein and J. Gonglewski, eds., International Society for Optics and Photonics (SPIE, 2012), pp. 137 – 149.

16. S. Gladysz, "Estimation of turbulence strength directly from target images," in *Imaging and Applied Optics*, (Optical Society of America, 2013), p. JW1A.4.
17. O. von der Lühe, "Estimating fried's parameter from a time series of an arbitrary resolved object imaged through atmospheric turbulence," *J. Opt. Soc. Am. A* **1**, 510–519 (1984).
18. F. Molina-Martel, R. Baena-Gallé, and S. Gladysz, "Fast PSF estimation under anisoplanatic conditions," in *Optics in Atmospheric Propagation and Adaptive Systems XVIII*, vol. 9641 K. U. Stein and J. D. Gonglewski, eds., International Society for Optics and Photonics (SPIE, 2015), pp. 141 – 151.
19. S. Basu, J. E. McCrae, and S. T. Fiorino, "Estimation of the path-averaged atmospheric refractive index structure constant from time-lapse imagery," *Proc. SPIE* **9465**, 94650T–94650T–9 (2015).
20. J. E. McCrae, S. Basu, and S. T. Fiorino, "Estimation of atmospheric parameters from time-lapse imagery," *Proc. SPIE* **9833**, 983303–983303–8 (2016).
21. E. J. Kelmelis, S. T. Kozacik, and A. L. Paolini, "Practical considerations for real-time turbulence mitigation in long-range imagery," *Opt. Eng.* **56**, 1 – 12 (2017).
22. R. C. Hardie, J. D. Power, D. A. LeMaster, D. R. Droegge, S. Gladysz, and S. Bose-Pillai, "Simulation of anisoplanatic imaging through optical turbulence using numerical wave propagation with new validation analysis," *Opt. Eng.* **56**, 1 – 16 (2017).
23. D. Fraser, G. Thorpe, and A. Lambert, "Atmospheric turbulence visualization with wide-area motion-blur restoration," *J. Opt. Soc. Am. A* **16**, 1751–1758 (1999).
24. R. C. Gonzalez and R. E. Woods, *Digital Image Processing (3rd Edition)* (Prentice-Hall, Inc., Upper Saddle River, NJ, USA, 2006).
25. A. V. Oppenheim and R. W. Schaffer, *Discrete-time Signal Processing (3rd Ed.)* (Prentice-Hall, Inc., Upper Saddle River, NJ, USA, 2010).
26. D. L. Fried, "Varieties of isoplanatism," *Proc. SPIE* **0075**, 20–29 (1976).
27. K. A. Winick and D. vL. Marquis, "Stellar scintillation technique for the measurement of tilt anisoplanatism," *J. Opt. Soc. Am. A* **5**, 1929–1936 (1988).
28. A. Schwartzman, M. Alterman, R. Zamir, and Y. Y. Schechner, "Turbulence-induced 2d correlated image distortion," in *2017 IEEE International Conference on Computational Photography (ICCP)*, (2017), pp. 1–13.
29. J. W. Goodman, *Introduction to Fourier Optics* (Roberts and Company Publishers, 2004), 3rd ed.
30. D. H. Tofsted, "Analytic improvements to the atmospheric turbulence optical transfer function," in *Targets and Backgrounds IX: Characterization and Representation*, vol. 5075 W. R. Watkins, D. Clement, and W. R. Reynolds, eds., International Society for Optics and Photonics (SPIE, 2003), pp. 281 – 292.
31. D. H. Tofsted, "A re-analysis of short-exposure turbulent effects on passive imaging," in *Atmospheric Propagation VII*, vol. 7685 L. M. W. Thomas and E. J. Spillar, eds., International Society for Optics and Photonics (SPIE, 2010), pp. 34 – 43.
32. D. H. Tofsted, "Reanalysis of turbulence effects on short-exposure passive imaging," *Opt. Eng.* **50**, 1 – 9 (2011).
33. R. L. Van Hook and R. C. Hardie, "Patch-based Gaussian mixture model for scene motion detection in the presence of atmospheric optical turbulence," in *Automatic Target Recognition XXX*, vol. 11394 R. I. Hammoud, T. L. Overman, and A. Mahalanobis, eds., International Society for Optics and Photonics (SPIE, 2020), pp. 227 – 238.
34. E. Agustsson and R. Timofte, "Ntire 2017 challenge on single image super-resolution: Dataset and study," in *The IEEE Conference on Computer Vision and Pattern Recognition (CVPR) Workshops*, (2017).
35. "University of Southern California Vol. 3: Miscellaneous," Available at <http://sipi.usc.edu/database/>.
36. B. D. Lucas and T. Kanade, "An iterative image registration technique with an application to stereo vision," in *International Joint Conference on Artificial Intelligence, Vancouver*, (1981).
37. Zhou Wang, A. C. Bovik, H. R. Sheikh, and E. P. Simoncelli, "Image quality assessment: from error visibility to structural similarity," *IEEE Transactions on Image Process.* **13**, 600–612 (2004).
38. R. C. Hardie, M. M. Hayat, E. Armstrong, and B. Yasuda, "Scene-based nonuniformity correction with video sequences and registration," *Appl. Opt.* **39**, 1241–1250 (2000).